



**HAL**  
open science

## Formation of fog due to stratus lowering: An observational and modeling case study

Maroua Fathalli, C Lac, Frédéric Burnet, Benoit Vie

### ► To cite this version:

Maroua Fathalli, C Lac, Frédéric Burnet, Benoit Vie. Formation of fog due to stratus lowering: An observational and modeling case study. Quarterly Journal of the Royal Meteorological Society, 2022, 148 (746), pp.2299 - 2324. 10.1002/qj.4304 . hal-03795958

**HAL Id: hal-03795958**

**<https://hal.science/hal-03795958v1>**

Submitted on 4 Oct 2022

**HAL** is a multi-disciplinary open access archive for the deposit and dissemination of scientific research documents, whether they are published or not. The documents may come from teaching and research institutions in France or abroad, or from public or private research centers.

L'archive ouverte pluridisciplinaire **HAL**, est destinée au dépôt et à la diffusion de documents scientifiques de niveau recherche, publiés ou non, émanant des établissements d'enseignement et de recherche français ou étrangers, des laboratoires publics ou privés.

**RESEARCH ARTICLE**

# Formation of fog due to stratus lowering: An observational and modelling case study

**M. Fathalli**  | **C. Lac**  | **F. Burnet**  | **B. Vié**CNRM, Université de Toulouse,  
Météo-France, CNRS, Toulouse, France**Correspondence**Maroua Fathalli, CNRM, Université de  
Toulouse, UMR 3589,  
Météo-France/CNRS, 42 avenue Gaspard  
Coriolis, Toulouse, France.  
Email: mcfarq@ou.edu**Abstract**

We numerically investigate the processes responsible for a fog event formed by stratus cloud lowering, observed on December 1–2, 2016, during the experimental campaign in the northeast of France. The observations revealed a complex temporal evolution with stratus followed by a relatively drier period and then its reformation leading to fog formation by stratus lowering. Microphysical observations below a tethered balloon exhibit different vertical profiles of liquid water content and droplet concentration between the stratus and the fog formed below. A simulation at 100-m grid spacing reproduced the main observed characteristics of the cloud life cycle despite a time lag in stratus formation due to large-scale conditions. The advection of cloud water in the stratus and at its top appears crucial to feed the stratus lowering, resulting in radiative cooling, vertical transport, droplet sedimentation, evaporation, and cooling of the sub-cloud layer. The advection of cold or warm air in the lowest 250 m, mainly driven by fine-scale orographic circulations, impacts the fog formation due to stratus cloud lowering. When non-local conditions are favourable, the most important microphysical process to favour fog formation is the droplet sedimentation, leading to the cooling and moistening in the sub-cloud layer by evaporation. Droplet sedimentation appears more efficient when the droplet concentration is low, and a two-moment microphysical scheme more appropriate than a one-moment scheme to reproduce the observed variability of the droplet concentration. Given the predominance of non-local processes on this case study, a three-dimensional high-resolution model appears crucial to perform accurate forecasts of fog by stratus lowering.

**KEYWORDS**

fog, high-resolution modelling, microphysics, stratus lowering

## 1 | INTRODUCTION

Fog is a meteorological phenomenon characterized by reduced horizontal visibility to less than 1 km due to

the presence of suspended water droplets (American Meteorological Society, 2017). Such weather conditions are a major concern for traffic safety, in particular for airports, causing significant financial losses (Pearson *et al.*, 2009).

Fog is also the second most likely cause of weather-related accidents (Gultepe *et al.*, 2019).

The most studied type of continental fog is radiation fog, forming by surface radiative cooling under clear skies. Another type of continental fog as prevalent as radiative fog is stratus cloud lowering (STL) fog, also called cloud-base-lowering fog, a result of the lowering of a pre-existing low stratus cloud to ground level (e.g., Price, 2011). STL fog differs from radiation fog by being already thick when fog forms at the surface. In this case, the formation phase consists of an interaction between the stratus and the sub-cloud layer instead of the radiative cooling of a stable layer. At Paris-Charles de Gaulle airport, radiative fogs and stratus-lowering fogs are the major fog types observed in equal proportions (Roquelaure *et al.*, 2009).

Despite a long history of fog research, numerical weather prediction (NWP) models still have problems simulating fog properly (e.g., Steeneveld *et al.*, 2015; Boutle *et al.*, 2022). Philip *et al.* (2016) found that the Météo-France operational model AROME simulated about 70% of radiative fogs and 30% of STL fogs at Paris-Charles de Gaulle airport. Difficulties in predicting STL are partly explained by an insufficient understanding of the phenomenon. Indeed, a better understanding of the phenomenon would allow the identification of the processes to be better represented in NWP models. Therefore, better forecasting requires first of all a better understanding of the main processes driving the STL.

The processes involved in the stratus lowering are illustrated in Figure 1. STL fog has been exhaustively studied in coastal areas where several field campaigns were carried out, especially in Europe and North America (e.g., Fernando *et al.*, 2021; Wagh *et al.*, 2021). The pioneer studies (e.g., Oliver *et al.*, 1978, Pilié *et al.*, 1979) found that radiative cooling from the stratus top is a primary driver of turbulence, inducing an increase of droplets diameter by collection processes. It enhances droplet sedimentation, moistening, and cooling of the sub-cloud layer by evaporation of droplets, propagating the stratus base downwards.

Koracin *et al.* (2001) suggested that, in addition to radiative cooling at the cloud top, large-scale subsidence is also an important factor for sea fog formation, as it acts to strengthen the inversion above the cloud top and force the cloud lowering.

However, STL fog over continental surfaces lacks baseline studies. Dupont *et al.* (2012), focusing on a 6-day period alternating between stratus and stratus-lowering fog in the Parisfog (Haefelin *et al.*, 2010) experiments, identified the humidification of the sub-cloud layer by evaporation of droplets falling from the cloud base as a key process for the formation of STL fog. More recently, Toledo *et al.* (2021) have applied a conceptual model based on adiabatic clouds to explain STL fog formation: The fog forms when the liquid water path (LWP) exceeds a critical value, forcing the cloud base to reach the ground to fill the layer between the cloud top and the ground. But this approach assumes cloud adiabaticity and is based on a column model, not including non-local effects.

To address this issue, this study investigates the complexity of local and non-local processes involved in an STL event combining experimental and numerical approaches. The case study analysed here has been observed during a field experiment over a hilly terrain. Observations include precise vertical profiles of the microphysical parameters using a tethered balloon. Previous numerical studies, such as Ducongé *et al.* (2020), have shown that a good compromise between large-eddy simulations, which cannot be run over large domains due to computation limitations, and meso-scale simulations, which do not resolve local circulations, is to use high-resolution mesoscale simulations (Cuxart, 2015) of about 100 m horizontal grid lengths to capture the valleys and the thermally driven flows (Vosper *et al.*, 2013; Smith *et al.*, 2021). Thus, a high-resolution mesoscale simulation is used here to conduct a process study relying on budgets of cloud water and potential temperature. Furthermore, as microphysical processes play an important role in STL fog formation (cloud droplet sedimentation and evaporation), additional simulations will

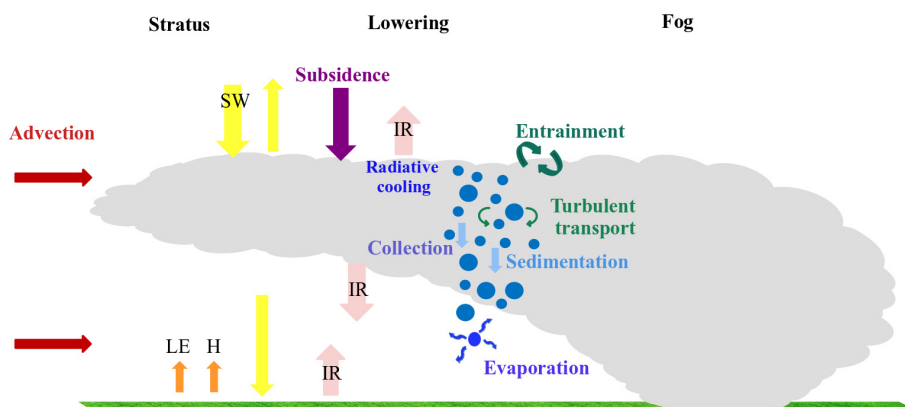


**FIGURE 1** Schematic representation of processes involved in stratus lowering up to fog formation [Colour figure can be viewed at [wileyonlinelibrary.com](http://wileyonlinelibrary.com)]

help assess the sensitivity of STL fog to microphysical processes and the benefit of a prognostic cloud droplet number in a two-moment microphysical scheme.

To our knowledge, this is the first processes study of a continental STL based on observation and high-resolution simulation. The article is organized as follows: Section 2 outlines the field campaign and the numerical set-up. Section 3 provides an overview of the case studied and the validation of the simulation by comparison with observations. In Section 4, a numerical analysis based on budgets is performed to better understand the processes leading to stratus lowering. In Section 5, sensitivity tests are conducted to quantify the impact of the microphysical scheme on stratus lowering, as well as to evaluate the impact of sedimentation and rain evaporative cooling. A discussion of the results is presented in Section 6, followed by conclusions and outlook in Section 7.

## 2 | EXPERIMENTAL DESIGN AND MODEL DESCRIPTION

### 2.1 | Measurements set-up

The selected stratus-lowering fog was observed on the night of December 1–2, 2016, during a field experiment carried out at the ANDRA's (the French national radioactive waste management agency) atmospheric platform located in Houdelaincourt, in the northeast of France (Tav *et al.*, 2018).

The main instrumented area ( $48.56^\circ$  N,  $5.50^\circ$  E), hereafter referred to as OPE, was located at the top of a small hill, 395 m above sea level (asl), covered with grassland and surrounded by grass and crops fields. Table 1 provides the list of the instruments used in this study.

Numerous instruments provide meteorological measurements at the surface and at different levels above the ground (10, 50, and 120 m). Two Present Weather Detector PWD22s measuring visibility were installed at 10 and 120 m, and a particulate volume monitor measuring liquid water content (LWC) and particle surface area was installed at 50 m. A secondary site in the valley located at 309 m asl (Figure 2), hereafter referred to as Valley, was equipped with a standard meteorological station and a PWD22.

At OPE, dry aerosol particle size distributions were measured using a scanning mobility particle sizer for particle diameters between 10.6 and 496 nm every 5 min, and an optical particle counter for particle diameters between 0.25 and 32  $\mu\text{m}$ . Remote-sensing instruments were also deployed to monitor continuously the cloud characteristics: a Vaisala CL31 ceilometer and an RPG HATPRO microwave radiometer to measure the cloud base height (CBH) and the LWP respectively (Martinet *et al.*, 2020).

During this event, three Vaisala RS92 radiosondes were launched at different times during the fog life cycle (2300 UTC on December 1, 0900 and 1200 UTC on December 2). Finally, in-situ vertical profiles up to 500 m were performed with a 18 m<sup>3</sup> tethered balloon equipped with meteorological sensors, a Gill ultrasonic anemometer and inertial sensor for turbulence measurements (Canut *et al.*, 2016), and an adapted DMT cloud droplet probe (CDP) to provide the size distribution of cloud droplets from 2 to 50  $\mu\text{m}$  in diameter at 1 Hz. The CDP was mounted on a wind vane to align the sampling section perpendicular to the wind. In addition, a small fan fixed just to the rear of the laser beam aspirates the air flow. The air speed in the sampling section is therefore equal to the wind speed plus 5 m·s<sup>-1</sup>. This formula has been empirically

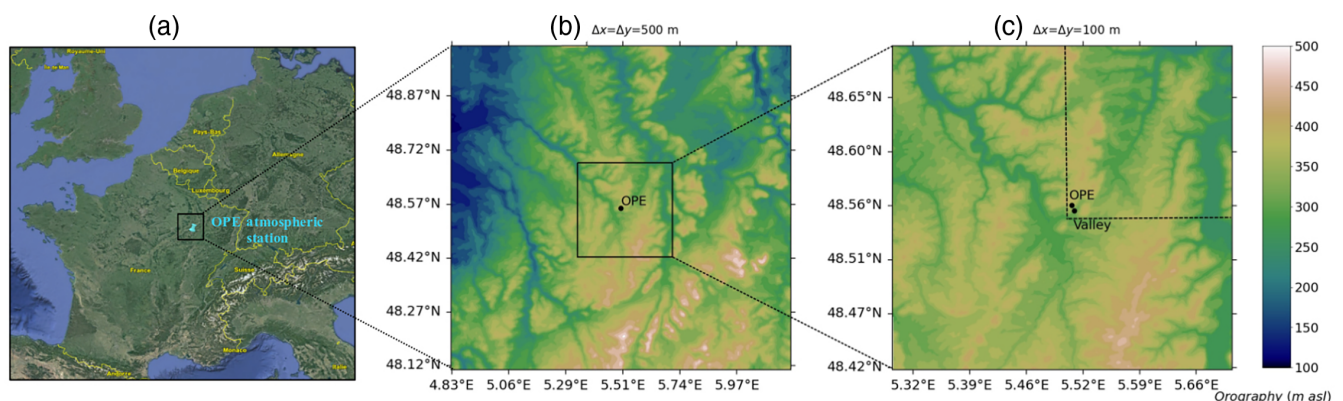


**FIGURE 2** (a) Geographical location of the OPE atmospheric station (©Google). Domains used for (b) the 500 m simulation and (c) the 100 m simulation. The black square in (b) indicates the nested 100 m domain in (c) centred over the OPE station. The black dots correspond to the two measurement locations. The colour shading represents the orography in metres above sea level (m asl). The dashed lines in (c) mark the zoomed region considered in Figure 15 [Colour figure can be viewed at [wileyonlinelibrary.com](http://wileyonlinelibrary.com)]

TABLE 1 Table of instruments that were deployed during the intensive observing period (IOP) and used in this study

Instrument	Measured variable	Vertical position	Measurement uncertainty	Temporal resolution
<b>Remote sensing</b>				
Vaisala CL31 ceilometer	Cloud base height (m) from 0 to 7.5 km		Greater of 1% or 5 m	30 s
HATPRO microwave radiometer	Liquid water path ( $\text{g}\cdot\text{m}^{-2}$ )		$20 \text{ g}\cdot\text{m}^{-2}$	5 min
Kipp Zonen CNR1	Downward long-wave radiation ( $\text{W}\cdot\text{m}^{-2}$ )		10% for daily sums	1 min
<b>In-situ microphysics</b>				
<b>In-situ microphysics</b>				
Vaisala PWD22	Horizontal visibility (m) from 0.01 to 20 km	10 and 120 m	10% (below 10 km)	1 min
Gerber PVM-100 (particulate volume monitor)	LWC ( $\text{g}\cdot\text{m}^{-3}$ ) and PSA ( $\text{cm}^2\cdot\text{m}^{-3}$ ) Aerosols	50 m	15% for both LWC and PSA	1 s
<b>Aerosols</b>				
Grimm EDM180 OPC (optical particle counter)	Dry aerosol number distribution from 0.25 to $32 \mu\text{m}$	2 m	10% uncertainty in diameter	1 min
TSI model 3096 SMPS (scanning mobility particle sizer)	Aerosol distribution from 10.6 to 496 nm Atmospheric profile IOP	2 m	5% uncertainty in diameter	2 min 30 s
<b>Atmospheric profile IOP</b>				
Vaisala RS92 radiosonde	Temperature ( $^{\circ}\text{C}$ )		$0.5^{\circ}\text{C}$	1 s
	Relative humidity (%)		5%	1 s
DMT cloud droplet probe	Droplet distribution from 2 to $50 \mu\text{m}$		30%	1 s

determined from comparison with measurements from the instrumented mast and with a Fog-Monitor also manufactured by DMT.

This fog case can be considered as a warm fog, as the observed temperature profiles were positive throughout the fog layer. Unless explicitly mentioned, all altitudes given in this article correspond to height above the ground level.

## 2.2 | Numerical set-up

The numerical simulations are performed with the non-hydrostatic atmospheric research model Meso-NH (Lac *et al.*, 2018), which has already been widely used for high-resolution simulations of fog (Bergot *et al.*,

2015; Bergot, 2016; Mazoyer *et al.*, 2019; Ducongé *et al.*, 2020). Here, a downscaling method is applied from the Météo-France operational model AROME (Seity *et al.*, 2011; Brousseau *et al.*, 2016) analyses at 1.3 km horizontal grid spacing, used for initial and hourly coupling conditions at boundaries of a 500 m horizontal grid spacing model over a domain size of  $100 \text{ km} \times 100 \text{ km}$ . The 100 m horizontal grid spacing model, over  $30 \text{ km} \times 30 \text{ km}$  centred on the observation site (OPE), is nested inside in a two-way interactive mode (Figure 2). In the vertical, 150 levels are used between the ground and the top of the model at 3,250 m for the two nested domains. The vertical grid spacing is 1.5 m for the first 50 m nearest the surface and is stretched above this level up to 50 m at the top of the model. A nudging to large-scale dynamical and thermodynamical fields from analyses is imposed above

2,850 m height above ground through an absorbing layer where the prognostic variables are relaxed towards the large-scale fields.

The advection scheme for momentum variables is a centred scheme of fourth order with a Runge–Kutta time-splitting of fourth order in time, whereas scalar variables are transported with the piecewise parabolic method scheme Colella and Woodward (1984).

The atmospheric model is coupled with the Interaction between Soil Biosphere and Atmosphere surface scheme (Noilhan and Planton, 1989) through the Externalized Surface model (Masson *et al.*, 2013). The orography data come from the Shuttle Radar Topography Mission with a resolution of 90 m for the 500 m model and 30 m for the 100 m model. The ECOCLIMAP database at 1 km resolution is used to generate land cover and surface parameters. Although the vegetation database resolution is coarser than the grid length, one can consider that it is not crucial as vegetation heterogeneities probably have no impact on the stratus lowering. The turbulence scheme is based on a prognostic equation for the turbulent kinetic energy (Cuxart *et al.*, 2000), in a one-dimensional mode with the Bougeault and Lacarrere (1989) mixing length at 500 m grid length and in a three-dimensional mode with the Deardorff (1980) mixing length at 100 m, well adapted to these resolutions.

Two microphysical schemes are used in this study: the one-moment scheme ICE3 (Pinty and Jabouille, 1998), which prognoses the mixing ratio of five hydrometeor species (cloud droplets, cloud ice, snow, rain, and graupel) and is currently used in the operational AROME model; and the two-moment Liquid Ice Multiple Aerosol (LIMA) scheme (Vié *et al.*, 2016), which inherits the ICE3 scheme. The main differences between the two schemes are prognostic concentrations of droplets, raindrops, and ice crystals for LIMA, whereas they are diagnostic in ICE3 with a constant number concentration (NC) for droplets; a prognostic evolution of the aerosol population for LIMA, with a detailed representation of aerosol–cloud interactions to handle competition between several cloud condensation nuclei (CCNs) modes, whereas aerosols are not represented in ICE3. In LIMA, each CCN mode is defined by its chemical composition, size distribution, and nucleation properties. The CCN activation parametrization following Cohard *et al.* (1998) is based on a diagnostic of maximum supersaturation  $S$ , which depends on vertical velocity, the growth of cloud droplets by condensation, and radiative cooling. In our study, the CCN activation parametrization in the LIMA scheme has been improved according to Vié *et al.* (2022) for general purpose by taking into account the growth of already available cloud droplets by condensation, limiting the overestimation of cloud droplet

activation. In ICE3, the parametrization of the warm auto-conversion is based on Kessler (1969) with a threshold for rain initiation of  $0.5 \times 10^{-3} \text{ kg}\cdot\text{m}^{-3}$  on the cloud water content. In LIMA, the rain formation rate depends on the cloud droplet size distribution following Berry and Reinhardt (1974) and Cohard and Pinty (2000). The droplet sedimentation is computed by considering the Stokes law for the cloud droplet sedimentation velocity, whereas fog deposition is not activated here as it does not impact the stratus lowering and the fog formation, which are the objectives of the study. There is no subgrid condensation scheme either as it becomes no longer necessary to be used at 100 m grid length according to Boutle *et al.* (2014). Furthermore, stratus clouds are not considered as subgrid clouds at this resolution.

The radiative transfer is computed with the European Centre for Medium-Range Weather Forecasts radiation code, with Fouquart and Bonnel (1980) for the short wave (SW) and the Rapid Radiation Transfer Model (Mlawer *et al.*, 1997) for the long wave (LW). Cloud optical properties are computed according to Martin *et al.* (1994) with the ICE3 scheme and according to Savijärvi *et al.* (1997) with the LIMA scheme by taking into account the prognostic cloud droplet concentration.

The simulation was initialized before any stratus has formed at 1500 UTC on December 1, 2016, from the AROME analyses, and lasted for 27 hr. The nested 100 m model is introduced at 1800 UTC. The time step is 1 s for the larger domain and 0.5 s for the smaller domain.

For the simulations using the LIMA scheme, three modes of aerosol were considered here according to aerosol in-situ measurements at OPE station, averaged over 1 hr before the appearance of the stratus. Concentrations and mean diameters of  $1,087 \text{ cm}^{-3}$  and 16 nm,  $3,960 \text{ cm}^{-3}$  and 64 nm, and  $0.444 \text{ cm}^{-3}$  and 875 nm are used for the Aitken, accumulation, and coarse modes respectively. The initial vertical distribution was set constant with height. The OPE station is a rural background site (Conil *et al.*, 2019; Farah *et al.*, 2020). As there was no information about their chemical nature, sulfate aerosols are assumed. Three simulations using LIMA are considered in this article:

- the reference simulation using LIMA, simulation hereafter denoted LIMA;
- LIMA without sedimentation of cloud droplets, denoted NOSED;
- LIMA without sedimentation of cloud droplets and without the cooling from the evaporation of raindrops, denoted NOSED + NOCOOL.

Two simulations were also performed with the ICE3 scheme using different droplet NCs of  $300 \text{ cm}^{-3}$  (denoted ICE3-300) and  $100 \text{ cm}^{-3}$  (denoted ICE3-100).

### 3 | OBSERVATIONS AND REFERENCE SIMULATION

#### 3.1 | Presentation of the observed case

##### 3.1.1 | Satellite observations

The night of December 1–2, 2016, was characterized by an anticyclonic circulation over France. Clouds products of NWC SAF of Eumetsat derived from Meteosat Second Generation satellite observations indicate the presence of a low cloud cover gradually expanding over the north-east of France and the OPE site between December 1 at 1800 UTC and December 2 at 1200 UTC (Figure 3, upper row). Additionally, the cloud type of low clouds is progressively replaced by very low clouds between 0600 and 1200 UTC, possibly representing the occurrence of fog by stratus lowering over a large area. Furthermore, cloud top

height (CTH) estimations indicate a rise of the cloud tops between 1800 and 0600 UTC at the OPE site, from approximately 800 to 1500 m asl (Figure 3, bottom row). The horizontal resolution of the satellite products is between 3 and 7 km.

##### 3.1.2 | Vertical structure

Vertical profiles of meteorological variables provided by three radiosondes launched from the OPE are depicted on Figure 4. At 2300 UTC (solid black line) there is a weakly stable stratus layer, about 400 m thick. The CBH is just below 100 m and we observe a strong inversion of temperature at the top of the stratus (+8 K over 150 m). Above, the atmosphere is very dry with vapour mixing ratios lower than  $0.5 \text{ g} \cdot \text{kg}^{-1}$  over more than 1 km.

At 0900 UTC (orange line) the stratus layer is much higher, with a cloud top at about 1400 m. Below, there is a 200 m thick fog in a stable layer, capped by an almost neutral subsaturated layer with a relative humidity of about 80% up to the cloud base at 900 m. It is noteworthy that, between 2300 and 0900 UTC, the layer between 550 and

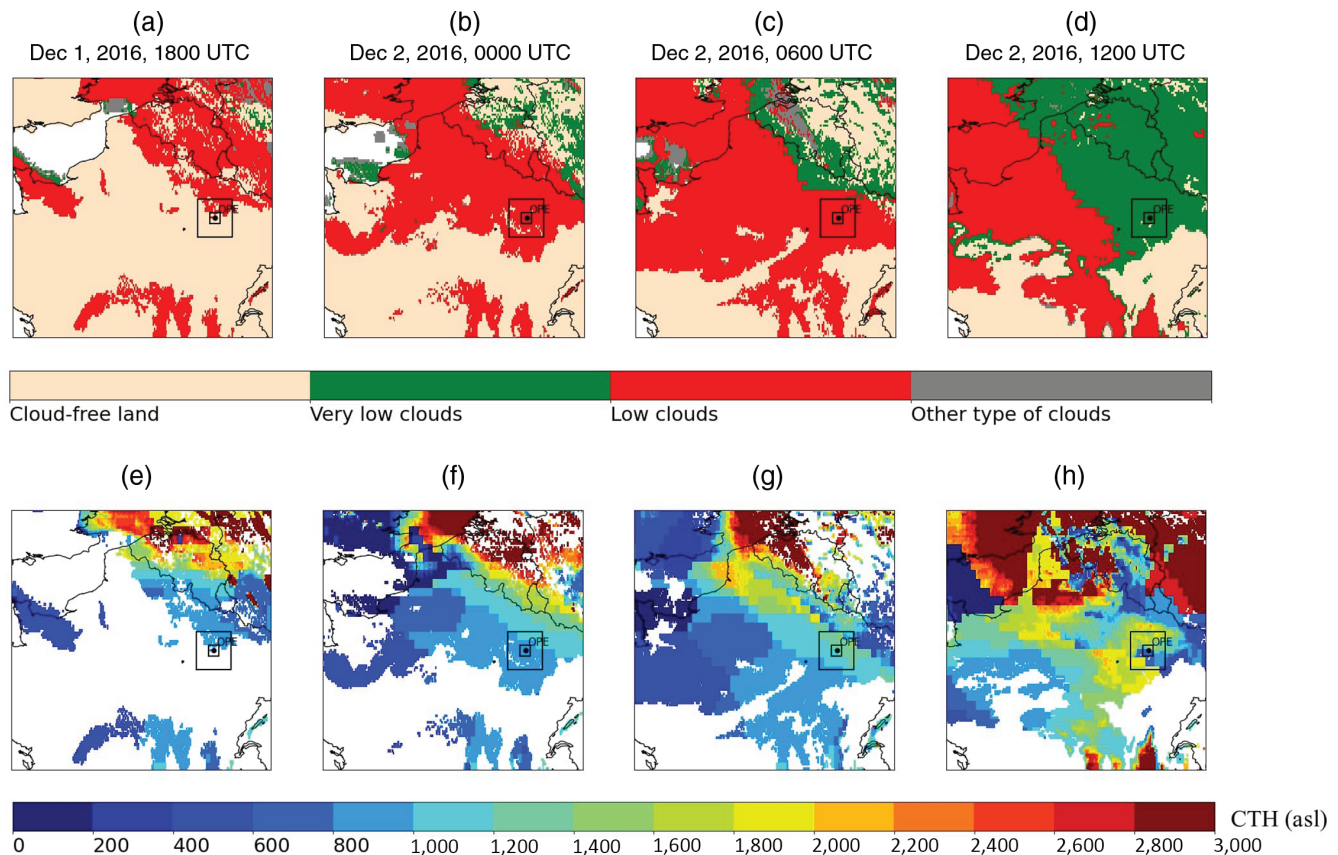


**FIGURE 3** Satellite observations of cloud type (top row) and cloud top height (CTH) above sea level (bottom row) derived from Meteosat Second Generation products of NWC SAF of Eumetsat during the night of December 1–2, 2016, at (a, e) 1800 UTC, (b, f) 0000 UTC, (c, g) 0600 UTC, and (d, h) 1200 UTC [Colour figure can be viewed at [wileyonlinelibrary.com](http://wileyonlinelibrary.com)]

1400 m experienced a significant cooling and moistening ( $-12$  K and  $+3$   $\text{g}\cdot\text{kg}^{-1}$  at 1300 m), whereas between 200 and 550 m the air temperature has warmed by about 3 K.

Finally, at 1200 UTC the fog has dissipated and a 200 m thick convective boundary layer has developed, capped by a slight inversion. Atmospheric properties above the inversion remain very similar, except that the stratus layer has also dissipated.

The wind speed is relatively uniform above 300 m at between 7 and  $10\text{ m}\cdot\text{s}^{-1}$ . There is a wind shear in direction that changes from northnortheast below the inversion layer to northwest above (not shown here). These radiosoundings thus indicate that the vertical structure has evolved from an initial low stratus at 2300 UTC to a more complex situation in the morning with three layers: a stratus much more elevated, a fog layer at the surface, and a subsaturated layer in between.

### 3.1.3 | Visibility at OPE and Valley sites

At the OPE station, fog is detected close to the surface (at 10 m) from 0548 to 1000 UTC (Figure 5). However, measurements at the elevated levels on the instrumented mast indicate a first drop of the visibility at 120 m just before 2200 UTC. In fact, measurements from the ceilometer reported in Figure 6 indicate that the initial stratus, which appeared at 1800 UTC with a CBH at about 300 m,

lowered below 100 m from about 1930 to 2330 UTC at the OPE. A drier period then followed with large fluctuations of the CBH detected by the ceilometer with values as high as 800 m (not shown), and a second stratus layer then appeared just before 0230 UTC with a CBH around 150 m. Visibility measurements indicate that the cloudy air then gradually lowered with a sharp drop of the visibility at 120 m at 0230 UTC, then at 50 m at 0400 UTC and a progressive decrease of visibility close to the surface up to the fog formation at 0548 UTC. Finally, at the Valley site 80 m below, fog occurred in the morning at 0800 UTC approximately 2 hr after the OPE site, following 3 hr of mist, and lasted 2 hr. According to Figure 5, fog dissipated at 1000 UTC at the surface and was lifted into low cloud.

The stratus arrival at 1800 UTC is depicted with a substantial increase of the downward long-wave radiation (LWD) from 240 to  $320\text{ W}\cdot\text{m}^{-2}$  and a gradual increase of the LWP that reached  $120\text{ g}\cdot\text{m}^{-2}$  at 2200 UTC (Figure 7). We note very low values of both LWP and LWD between 0030 and 0330 UTC, attesting that the two stratus events are separated by a drier period. Indeed, measurements with the tethered balloon (not shown) indicate that the initial stratus layer disappeared progressively from 0000 UTC with the advection of warmer and drier air; for instance, the air temperature at 250 m increased from  $0^\circ\text{C}$  at 2200 UTC to  $2.5^\circ\text{C}$  at 0200 UTC, whereas, below, the surface layer stabilized with a continuous decrease of the

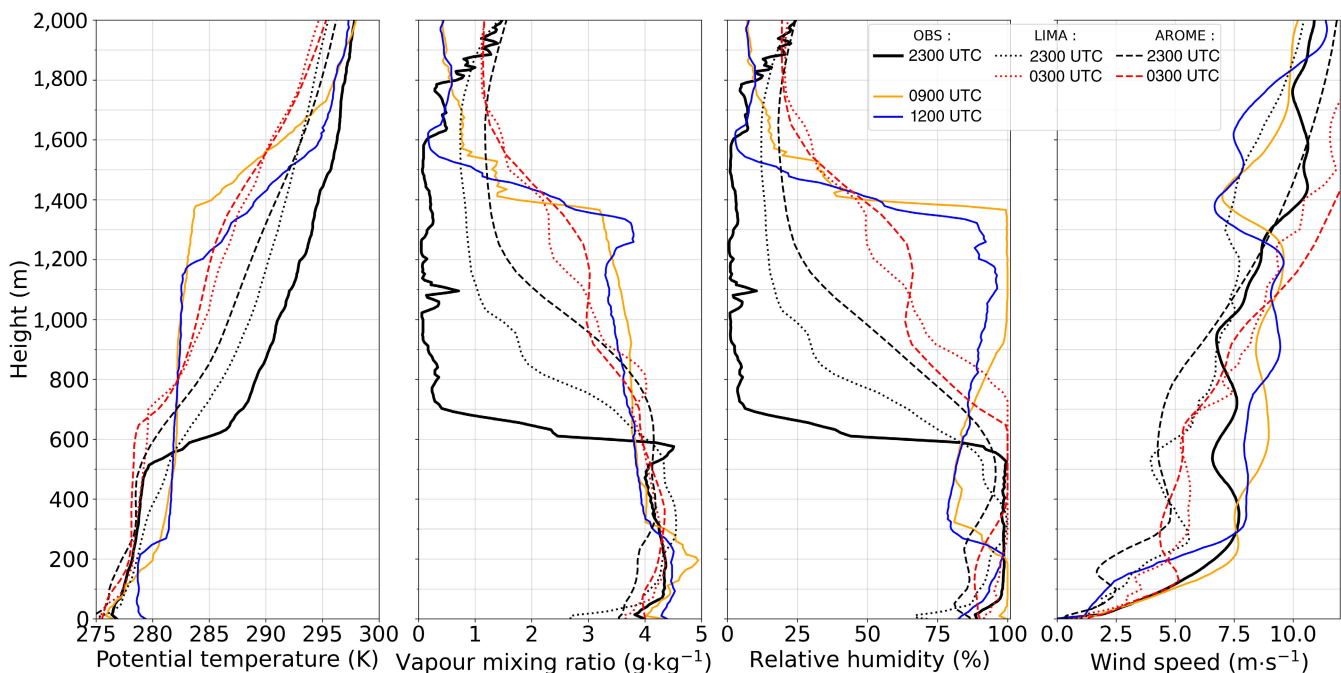


**FIGURE 4** Vertical profiles of potential temperature, vapour mixing ratio, relative humidity, and wind speed as measured by the radiosondes launched at OPE station at 2300, 0900, and 1200 UTC (solid lines); and simulated from the reference simulation (dotted lines) and the AROME analyses (dashed lines) at 2300 UTC (black) and 0300 UTC (red) [Colour figure can be viewed at [wileyonlinelibrary.com](http://wileyonlinelibrary.com)]

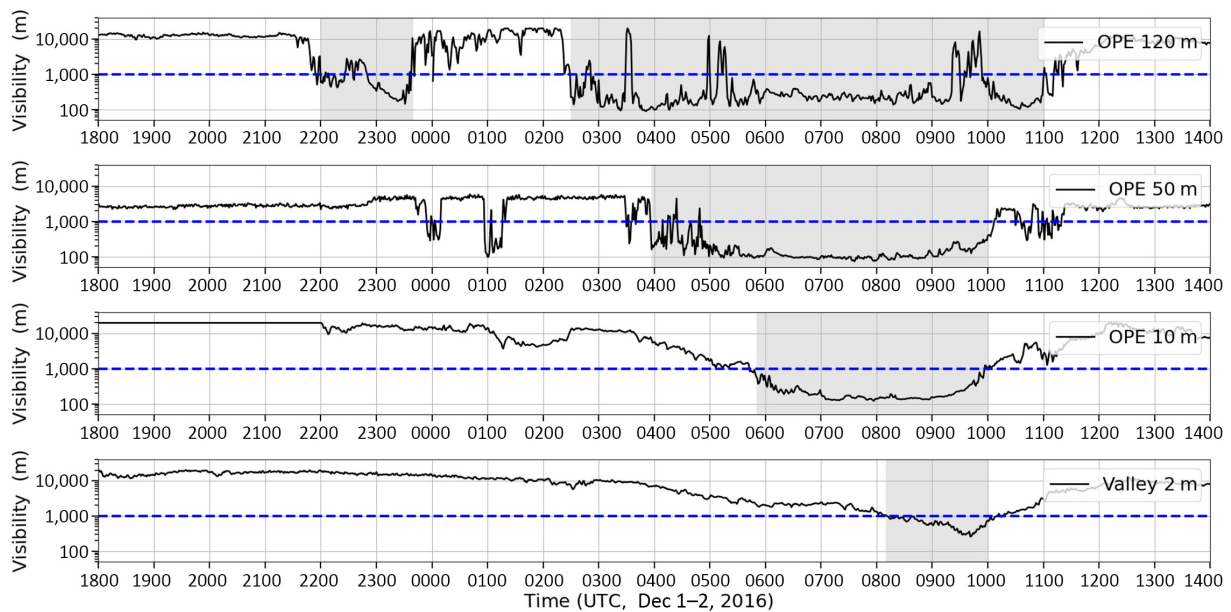


**FIGURE 5** Time series of visibility measurements from top to bottom at 120 m, 50 m, and 10 m at OPE and at 2 m at the Valley site. Visibility is derived from PVM100 data at 50 m. The horizontal blue dashed lines correspond to the cloudy air threshold (1,000 m), and the main periods of stratus and fog are indicated by the shaded areas [Colour figure can be viewed at [wileyonlinelibrary.com](http://wileyonlinelibrary.com)]

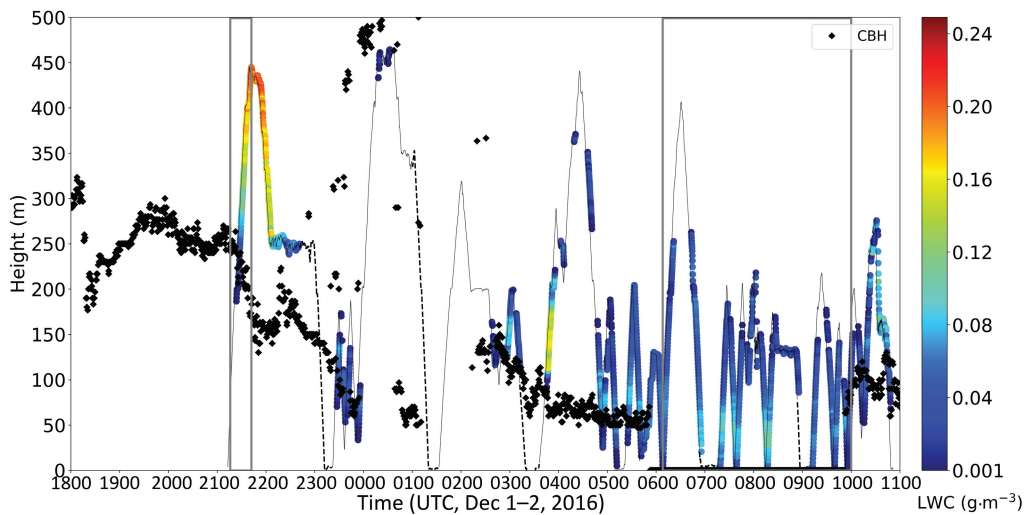


**FIGURE 6** Cloud base height (CBH, m) derived from the ceilometer (black diamond marker) and liquid water content (LWC) derived from the cloud droplet probe (CDP) measurements (coloured dot) superimposed on the tethered balloon path. Dashed line corresponds to time periods without CDP data when the battery was discharged. Each colour dot corresponds to the cumulative over 10 s of the CDP data. The CBH is set to zero during the fog (between 0548 and 1000 UTC) based on the visibility measurements at 10 m. The two rectangles indicate the time periods selected to compare vertical profiles of measurements with the simulations in Figure 9 [Colour figure can be viewed at [wileyonlinelibrary.com](http://wileyonlinelibrary.com)]

temperature within the first 100 m until fog formation at around 0600 UTC.

### 3.1.4 | Microphysical observations

The tethered balloon had a maximum ascent/descent speed of  $0.5 \text{ m} \cdot \text{s}^{-1}$ , resulting in a vertical spatial resolution

higher than 5 m. The CDP is powered with a battery that allows measurements up to a maximum of around 1.5 hr. A large variability of LWC values was observed during the flight periods (Figure 6). Indeed, the highest values of LWC ( $0.26 \text{ g} \cdot \text{m}^{-3}$ ) were recorded in the first stratus layer, whereas they were substantially lower in the fog layer. The first ascending vertical profile at 2110 UTC reveals

a continuous increase of LWC with height. The balloon sampled the stratus layer over 250 m thick but has to stop just below 450 m because of the authorized ceiling. This was likely very close the cloud top, which was detected just above 500 m by the radiosonde launched at 2300 UTC (Figure 4).

Around 2330 UTC, the balloon sampled very low stratus layers, which were also very thin (< 100 m thick), consistent with the measurements of the instrumented mast. The next ascending profiles confirmed that cloudy air had disappeared during the drier period, up to at least 450 m. Some thin stratus layers were further sampled at various altitude levels, with LWC values that could exceed  $0.14 \text{ g}\cdot\text{m}^{-3}$  over 100 m as measured during the ascent just before 0400 UTC. But when the cloudy air approached very close to the surface from 0440 UTC, the layer was about 200 m thick and LWC values did not exceed  $0.12 \text{ g}\cdot\text{m}^{-3}$ . Moreover during the fog event, similar low values of LWC were recorded with maximum values located around 50 m despite the 250 m fog layer depth around 0630 UTC. The fog layer reaches its minimum thickness of 100 m just before its dissipation as a stratus around 1000 UTC.

### 3.2 | Validation of the reference simulation

The performance of the reference simulation called LIMA will be examined first, by comparison with measurements at the OPE site.

Figure 4 compares the vertical profiles of the reference simulation (dotted black line) with the soundings at 2300 UTC and with the AROME analyses (dashed black lines). The stratus layer, already observed from 1800 UTC at OPE (Figure 6), is very thin in LIMA at 2300 UTC as it only beginning to appear, whereas it does not even exist yet in the AROME analyses. Consequently, the models underestimate the near-surface potential temperature (due to an excessive cooling) and vapour mixing ratio near the ground at 2300 UTC. This is reinforced by the underestimation of the wind speed in the whole 800 m layer. Additionally, inversion gradients are underestimated, with too cold and too moist air above the inversion in the analyses and the simulation.

If we consider the analysed and simulated profiles 4 hr later than the observation, they then become in better

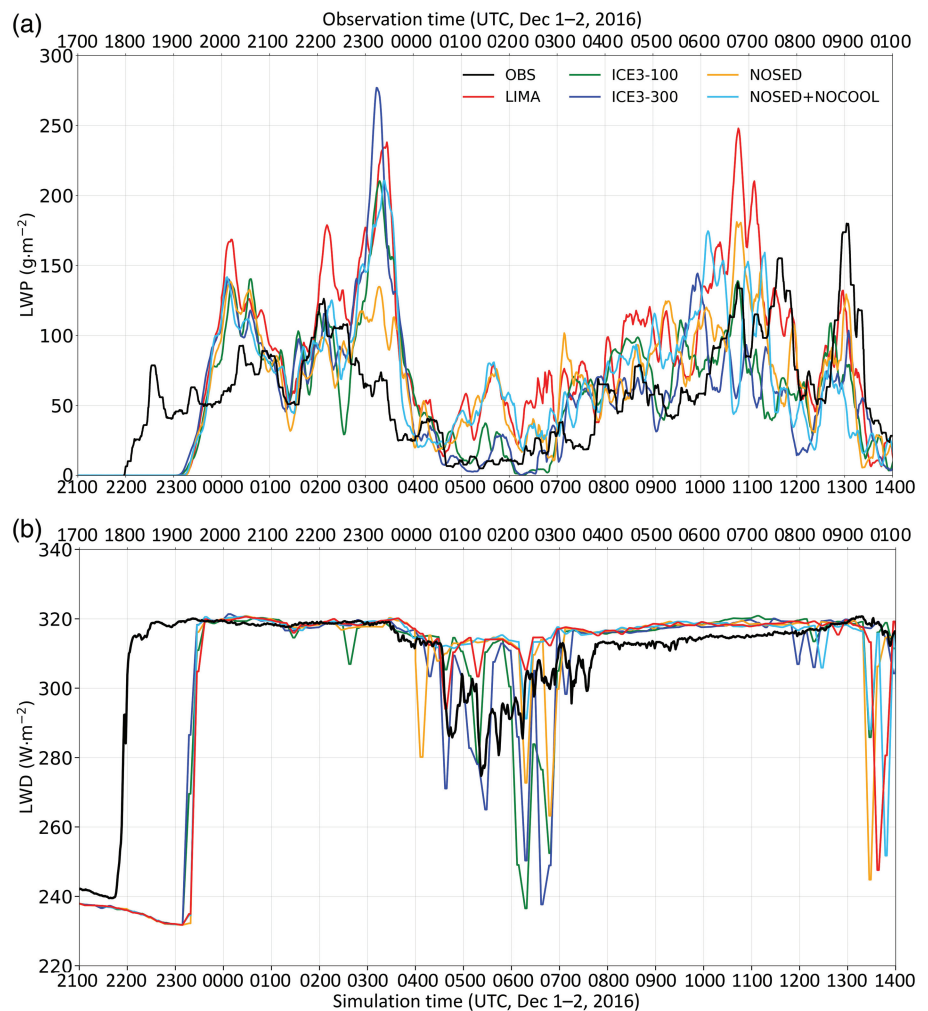


**FIGURE 7** Time series of the modelled and observed (a) liquid water path (LWP,  $\text{g}\cdot\text{m}^{-2}$ ) and (b) downward long-wave radiation (LWD) at 2 m ( $\text{W}\cdot\text{m}^{-2}$ ) [Colour figure can be viewed at [wileyonlinelibrary.com](http://wileyonlinelibrary.com)]

agreement with each other. The stratus layer is well developed, but the top of the stratus is 200 m higher in the simulation. Potential temperature and vapour mixing ratio profiles in the first 500 m are in good agreement between the reference simulation at 0300 UTC and the observations at 2300 UTC.

Owing to the delay in the formation of the stratus in the simulation, consecutive to the delay in the AROME analyses, we will introduce in the following parts a virtual time lag of 4 hr in the observations in order to study the stratus lowering in consistency between observation and simulation, but without delaying the sunrise in the model, which occurred at 0710 UTC. Therefore, Figures 7 and 8 present temporal evolutions of simulated fields compared with the observations with the real time axis of the measurements at the top and the time axis of the observations shifted by 4 hr at the bottom of the figures, the latter corresponding to the time of the simulations. The simulated and observed LWPs correspond (rainwater excluded).

After considering this time lag of 4 hr in the observations, the simulated stratus is still formed 1 hr late, at 2300 UTC at 300 m above the ground and grows both downwards and upwards (Figure 8a). The cloud base lowers to 100 m at 0000 UTC without reaching the ground, and then it rises while the cloud top continues to propagate

upwards. At 0330 UTC, the cloud base lowers again until 80 m, which is consistent with the observed CBH, at which time the simulated LWP reaches  $230 \text{ g}\cdot\text{m}^{-2}$ , which is over-estimated compared with the observed value of  $70 \text{ g}\cdot\text{m}^{-2}$  (Figure 7a). These two missed opportunities to form fog will be discussed later.

Between 0400 and 0600 UTC, the cloud thickness is strongly reduced through an increase in the CBH, in agreement with the observed CBH. The simulated LWP is also reduced, reflecting the observations, but it remains over-estimated by around  $30 \text{ g}\cdot\text{m}^{-2}$ . The drier period is thus almost correctly simulated. After 0600 UTC, the stratus lowers again when the LWP increases, reaching the ground at 1000 UTC, this time simultaneously with the observations (always considering the virtual time lag). The simulated fog dissipates after 1200 UTC, in advance compared with the observations, but the delay in the stratus formation induces diurnal surface fluxes favouring the dissipation of the fog, whereas they remain earlier in the morning and so are weaker in the observations. We will therefore not study the fog dissipation phase, in agreement with the objective of the study to focus on stratus lowering and fog formation.

Considering the virtual time lag, the temporal evolution of the simulated CBH is fairly well reproduced,

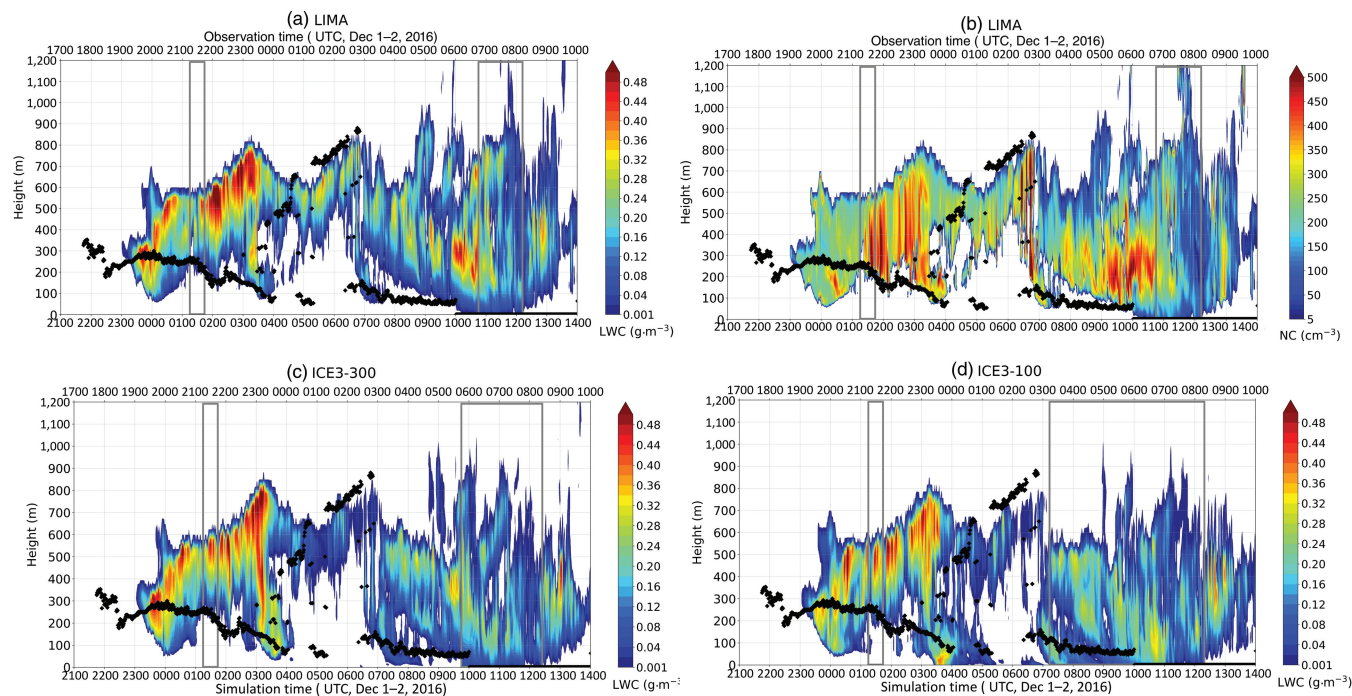


**FIGURE 8** Temporal evolution of vertical profiles at OPE of (a) liquid water content (LWC,  $\text{g}\cdot\text{m}^{-3}$ ), (b) droplet number concentration (NC,  $\text{cm}^{-3}$ ) for the LIMA simulation, and LWC for (c) ICE3-300 and (d) ICE3-100. The real time axis of the measurements is at the top of the figures, and the time axis of the observations shifted by 4 hr corresponding to the time of the simulations is at the bottom of the figures. Measurements of cloud base height are superimposed in black dots. Rectangles indicate the time periods selected to compare with vertical profiles of measurements in Figure 9 [Colour figure can be viewed at [wileyonlinelibrary.com](http://wileyonlinelibrary.com)]

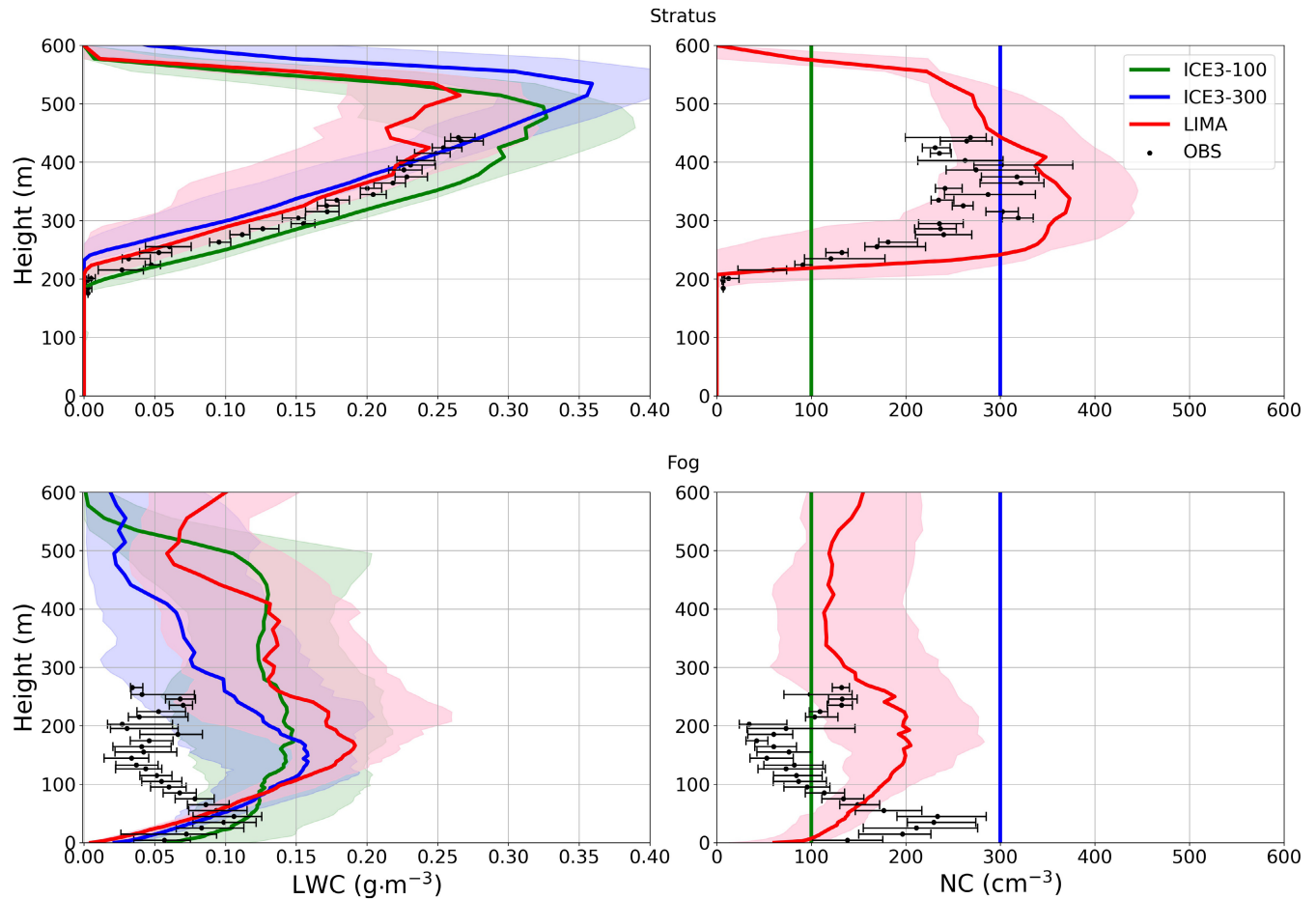


**FIGURE 9** Vertical profiles of (a, c) the liquid water content (LWC,  $\text{g}\cdot\text{m}^{-3}$ ) and (b, d) droplet number concentration (NC,  $\text{cm}^{-3}$ ) calculated from the cloud droplet probe (CDP) measurements under tethered balloon (black dots), simulated by LIMA (red line), ICE3-100 (green line), and ICE3-300 (blue line). Profiles (a) and (b) were recorded during the stratus phase, whereas profiles (c) and (d) were recorded during the fog period. The CDP data are averaged over an altitude interval of 10 m. The shaded area and horizontal error bars denote the first (25%) and third (75%) interquartile ranges averaged over 22 min for the stratus layer and over the fog period for each simulation. Median values are indicated by the dots for the observations and solid line for simulations [Colour figure can be viewed at [wileyonlinelibrary.com](http://wileyonlinelibrary.com)]

despite a few discrepancies. The rate of cloud base lowering between 0700 and 1000 UTC exhibits a slightly smaller value. It should be noted that the ceilometer has a blind zone in the first 50 m. With regard to the CTH, there is no cloud radar observation, but the increase of the CTH is confirmed by satellite data products, exhibiting a CTH around 400 m, 500 m, 800 m, and 1200 m at 1800 UTC, 0000 UTC, 0600 UTC (Figure 3), and 0900 UTC respectively, and by the radiosounding profiles at 2300 UTC and 0900 UTC giving a CTH of 550 m and 1400 m respectively (Figure 4), in the observation temporal baseline.

Up to 0300 UTC, the LWD flux is well reproduced with an almost constant value of  $320 \text{ W}\cdot\text{m}^{-2}$ , which is similar to the observations (Figure 7b). This means that the optical thickness of the stratus layer is well simulated, in accordance with the LWP (Figure 7a). During the drier period

between 0400 and 0600 UTC, the LIMA simulation overestimates the LWD in agreement with the overestimation of the LWP already mentioned. It should be noted that the temporal fluctuations of the observed LWD flux during the drier period are reproduced, due to the dissipation of the stratus in the observations and its thinning in the simulation.

The temporal evolution of the simulated LWC and concentration exhibits a substantial variability during the cloud life cycle, with higher values in the stratus than in the fog (Figure 8a,b). The main aerosol mode to be activated is the accumulation mode and peaks of activation are mainly linked to the maximum of vertical velocity (not shown). We can evaluate simulated microphysical fields by using the measurements with the tethered balloon when considering equivalent cloud phases (stratus and fog). For the stratus, we choose the first ascending

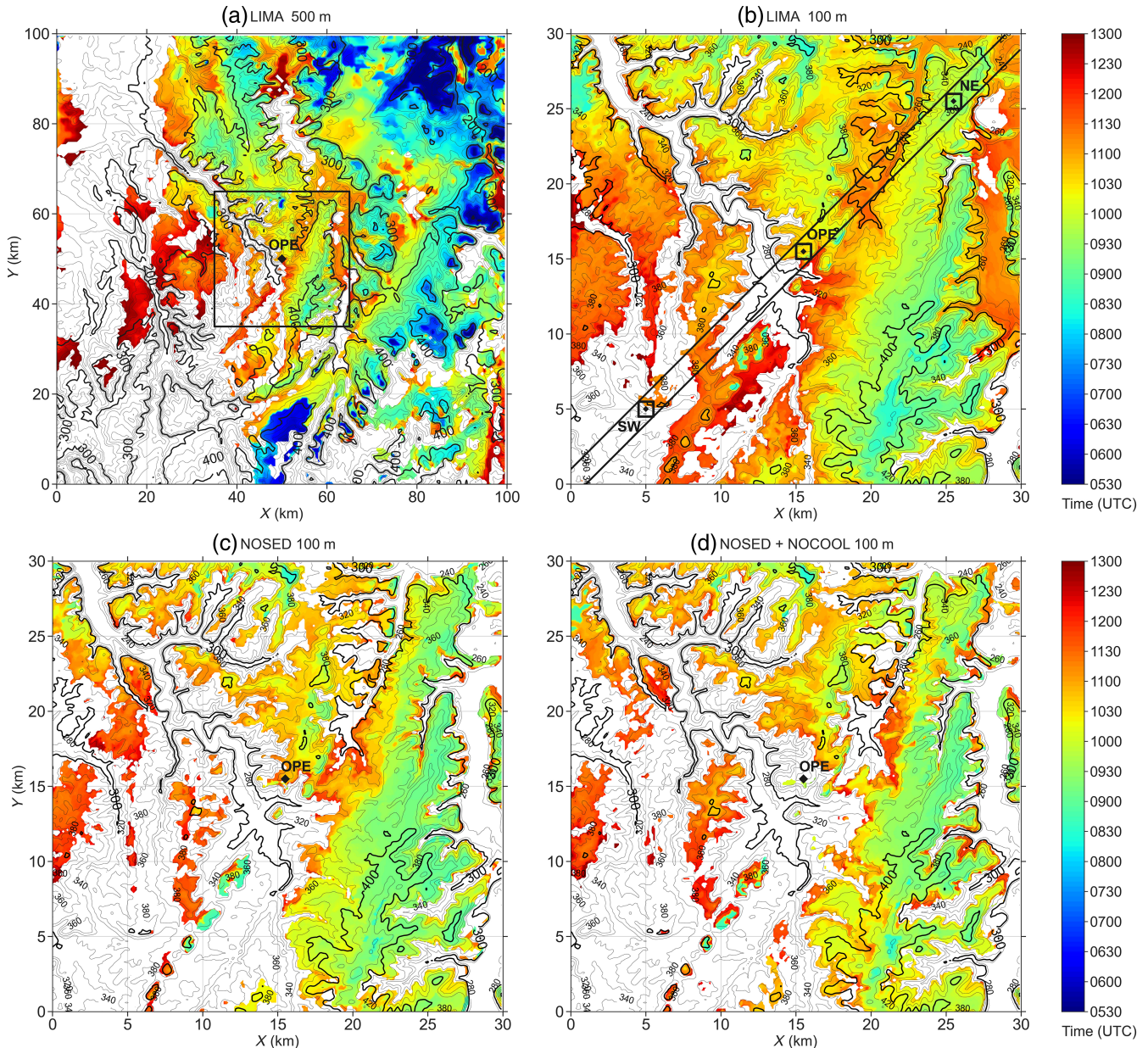


**FIGURE 10** Two-dimensional maps of fog onset time at ground level (time [UTC], colour shading) from the (a) 500 m and (b) 100 m horizontal resolution model for LIMA simulation, (c) NOSED, and (d) NOSED + NOCOOL simulations. Black contours represent the orography, from 100 to 500 m, every 20 m. In (b), the three sites are marked by black diamonds. Rectangles around these sites show the subdomains used to compute vertical profiles and budgets in Figure 13. The diagonal band will be used in Figure 11 [Colour figure can be viewed at [wileyonlinelibrary.com](http://wileyonlinelibrary.com)]

profile beginning at 2115 UTC (observation time) and lasting 22 min and compare it with the one at 0115 UTC (simulation time) averaged over the same period, whereas for the fog we average over the whole fog period in both observations and simulation (grey rectangles in Figures 6 and 8).

In the stratus, LIMA reproduces correctly the observed values, with a quasi-adiabatic vertical profile of LWC above the cloud base up to  $0.25 \text{ g}\cdot\text{m}^{-3}$  at 420 m, while droplet concentration increases up to  $350 \text{ cm}^{-3}$  within the first

50 m above the cloud base and remains almost constant above.

In contrast, in the fog, the simulated LWC and droplet NC values are strongly overestimated in the upper part of the fog layer. Indeed, simulated and observed profiles have almost the same shape in the lower part, but above 50 m altitude the simulated values continue to increase, reaching almost  $0.20 \text{ g}\cdot\text{m}^{-3}$  and  $200 \text{ cm}^{-3}$  respectively at 180 m, whereas they are decreasing with height in the observations up to about 200 m. Note, however, that the

simulation produces a fog layer much thicker than the observed one, with a CTH at about 800 m, which could explain part of the shape discrepancy. Moreover, median values of droplet NC measured around 50 m reach about  $220 \text{ cm}^{-3}$ , which is very similar to the simulated values. Despite these discrepancies, the main microphysical features of stratus and fog layers are then correctly reproduced by the LIMA scheme.

Other types of hydrometers, such as raindrops, ice crystals, snow aggregates, and graupel, are produced by the model as well as in AROME, but in very small amounts compared with the droplet water content (not shown). Although the temperature is positive at the ground, it becomes negative with height, explaining the presence of mixed hydrometers.

To conclude this part, despite the 4-hr delay due to the large-scale conditions, the LIMA simulation is in a fairly good agreement with the observations in terms of thermodynamical and microphysical conditions accompanying the stratus lowering. Therefore, this simulation will be used in the next section to explore the processes driving the stratus lowering for this case.

## 4 | ANALYSIS OF STRATUS CLOUD LOWERING

The previous section focused on the cloud evolution at the vertical of the OPE station in order to validate the reference simulation. We will now consider the simulation in its three-dimensional representation to characterize the differences between some points of the domain in terms of stratus lowering and to determine the main processes driving the stratus lowering and the fog formation.

### 4.1 | Two-dimensional representation

Figure 10 presents a two-dimensional representation of the fog onset time in both domains from 0530 to 1300 UTC, as there is no more fog formation after 1300 UTC. In the larger domain (500 m grid spacing), the formation of fog first occurs in the northeast at 0530 UTC, preferentially at the top of the hills, and propagates towards the southwest, always favouring areas of higher altitude. It does not reach the western part of the domain. In the inner domain (100 m grid spacing), the fog is first formed at 0825 UTC in the southeast of the domain, over the hills. Then it spreads northward along the crest and over the surrounding raised areas. In the northeast of the domain, the fog begins to form around 0940 UTC. After 1 hr, the fog appears at the OPE station. However, the

valley from the northwest to OPE remains free of fog, as well as most of the southwest area, although the area is at the same height as other locations where the fog formed. At the Valley site, the simulated stratus reaches the ground around 1200 UTC, almost 2 hr after the OPE site; the delay between the two sites is in agreement with the observations (Figure 5). In the inner domain, 75% of the area of the domain is covered by fog formation, and 87% of the regions where the altitude is higher than 330 m.

Orography and geographical positions, therefore, appear crucial for the stratus to reach the fog state during this event. We will use in the following parts the diagonal band from southwest to northeast, presented in Figure 10b, to analyse the scenario, as well as the three squares of  $1 \text{ km}^2$  located at an average altitude of 330 m called SW, OPE, and NE, included in this diagonal band.

### 4.2 | Vertical representation

Figure 11 displays the evolution of the cloud layer every hour from 0650 to 1150 UTC along the diagonal band and confirms that the stratus lowering is generalized over the domain, as well as the advection of boundary-layer clouds from the northeast to the southwest. For the three sites, the stratus begins to lower around 0750 UTC. Between 0750 and 0850 UTC, the cloud cover tends to deepen from its top and its base. At 0850 UTC, an advection of high cloud mixing ratio from the northeast feeds the cloud and contributes to lower the stratus. At 0950 UTC, the stratus reaches the ground at the NE site. The cloud first touches the top of the hill and then spreads towards the valley. About 1 hr later, the fog forms at the OPE site. Above the SW site, the stratus continues to lower but without reaching the ground.

### 4.3 | Link between LWP, CTH, and stratus lowering

To explain the occurrence of fog, Toledo *et al.* (2021) proposed a conceptual model by considering a critical LWP (noted CLWP) as the minimum amount of LWP that is necessary to fill a fog layer of a given thickness; the possibility for a very low stratus layer to deepen into fog corresponds to an LWP higher than this CLWP value. This approach assumes adiabaticity in the cloud and does not include three-dimensional effects like the horizontal advection. Therefore, we attempt to investigate how the LWP and CTH behave during the stratus lowering and whether a CLWP value is correlated to the fog occurrence.

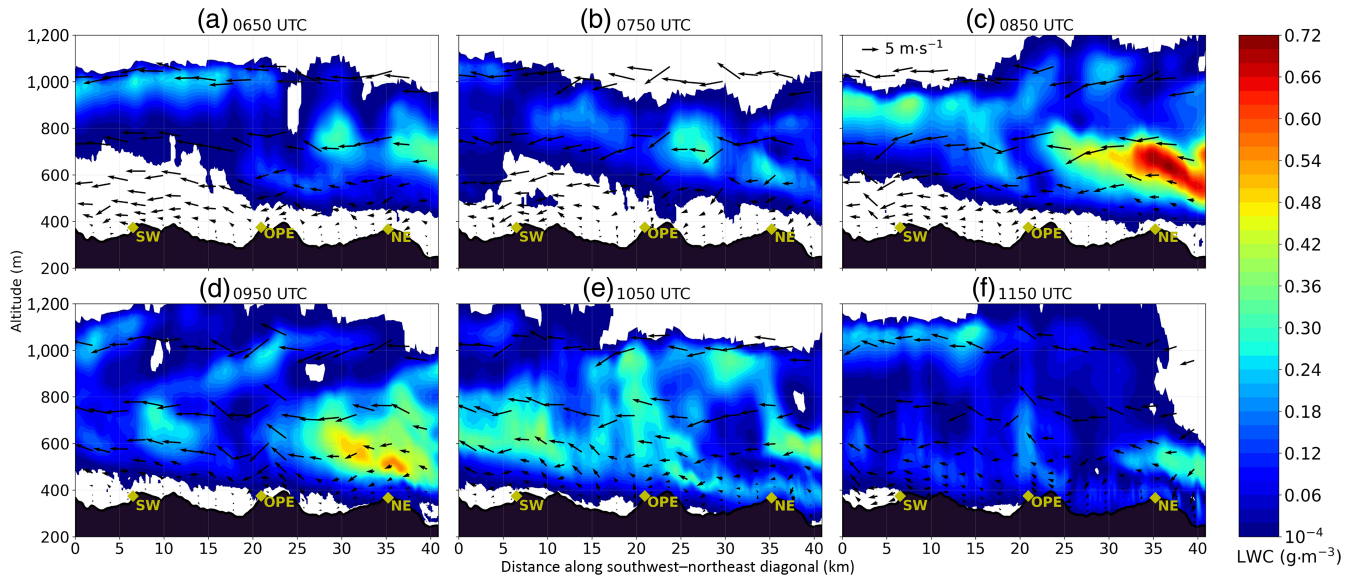


**FIGURE 11** Vertical cross-sections along the diagonal band presented in Figure 10b of simulated liquid water content (LWC,  $\text{g}\cdot\text{m}^{-3}$ ) every hour from 0650 UTC until 1150 UTC averaged during 5 min. The three sites are marked with yellow diamonds. The arrows represent the direction and the wind speed along the vertical cross-section [Colour figure can be viewed at [wileyonlinelibrary.com](http://wileyonlinelibrary.com)]

Before 0900 UTC, the variability of the CTH is low, with values less than 800 m (Figure 12a). The sudden increase of the CTH up to 1250 m appearing around 0900 UTC over the northeastern part, already underlined in Figure 11c, propagates towards the southwestern part with a velocity around  $6\text{ m}\cdot\text{s}^{-1}$  corresponding to the mean wind speed at this level. This increase of CTH is not impacted by the orography. It is followed 15 min after the formation of fog (red line) around the NE site, as well as around the OPE site after 30 min. Between these two sites and at the northeast of the NE site, the fog forms but later due to the valley topography. From OPE towards SW, the stratus reaches the ground at the peak preceding the SW location almost 1 hr after the increase of the CTH, but the fog does not form beyond.

Owing to the propagation of CTH and to the variability of the orography, we consider the LWP divided by the CTH above the ground level to get rid of these effects (Figure 12b), which we called the normalized LWP (NLWP), in order to represent the layer to be filled by the cloud water. In the first part of the night, two higher values of NLWP seem to stand out around 0000 and 0330 UTC with CBH below 100 m, but without leading to fog, in agreement with Figure 8a. Around 0900 UTC, the stratus appearing in the northeast of the domain is characterized by a higher NLWP, associated with a more marked propagation than the previous maxima. Around the NE site, the maximum of NLWP is followed almost immediately by the fog formation. High NLWP values tend to propagate towards the OPE area, but not continuously. Fog formation at the OPE site still occurs during a period with

high NLWP. On the contrary, fog formation between OPE and SW is not correlated with a strong value of NLWP, whereas strong values of NLWP around OPE at 0000 and 0330 UTC did not lead to fog. Therefore, it appears that a conceptual model based on a CLWP is not adapted to this fog event, meaning that the adiabaticity assumption is not respected here, because of other effects like horizontal transport or diabatic processes. We will come back to this point in Section 6. A further analysis based on thermodynamical variables budgets will now be conducted to highlight the horizontal transport and diabatic processes driving the stratus lowering.

#### 4.4 | Budget analysis

In order to better understand the processes leading to stratus lowering and why fog is formed in some places and not in others, a budget analysis of cloud mixing ratio ( $rc$ ), potential temperature, and vapour mixing ratio ( $rv$ ) has been performed over the three  $1\text{ km}^2$  squares mentioned before, NE, OPE and SW (Figure 10b). These three subdomains are positioned at the same altitude of 330 m and experience different scenarios of stratus lowering. Since our objective is to investigate stratus lowering, the budgets are averaged for each site over the stratus lowering period, which is defined as the period between the onset of stratus lowering and the fog formation, when it is reached or tends to be. The stratus lowering begins at almost the same time at the different sites, considered at 0750 UTC, but with different CBHs. The end of the period is 0920 and 1010 UTC

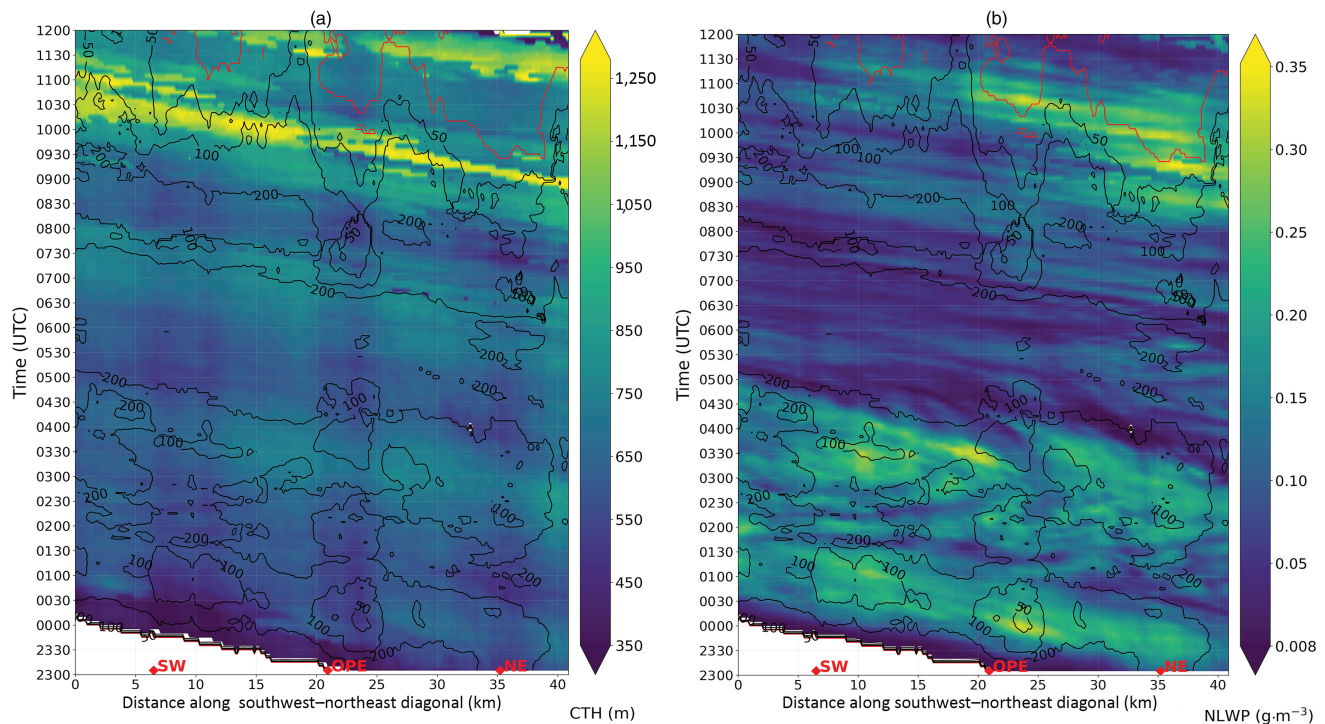


**FIGURE 12** Temporal evolution (in the model temporal scale) between 2300 UTC on December 1 and 1200 UTC on December 2, 2016 (y-axis) along the southwest–northeast diagonal (Figure 10b) (x-axis) of (a) the cloud top height (CTH, m) and (b) the normalized liquid water path (NLWP), defined as the LWP divided by the distance between the CTH and the ground altitude (presented in (a)). The red line represents the cloud base height (CBH) at 0 m (e.g., the fog formation), and the black lines the CBH at 100 and 50 m. The three sites are marked with a red diamond. The white color in (a) corresponds to clear sky [Colour figure can be viewed at [wileyonlinelibrary.com](http://wileyonlinelibrary.com)]

for the NE and OPE sites respectively, corresponding to the fog onset, whereas 1100 UTC is considered for SW without fog formation. The delay of 4 hr in the simulation compared with the observations induces heating by the ground, which slows down the formation of fog as the morning progresses. However, this does not impact significantly the analysis of the differences between the sites. Figure 13 presents vertical profiles of cloud mixing ratio and the budgets of cloud mixing ratio, potential temperature, and vapour mixing ratio during these periods for the three sites in order to conduct the process study.

#### 4.4.1 | NE subdomain

At NE, the stratus base lowers by 125 m from 0750 to 0920 UTC, when it touches the ground. Over this period of 1 hr 30 min, the maximum LWC increases from  $0.2 \text{ g}\cdot\text{kg}^{-1}$  to  $0.58 \text{ g}\cdot\text{kg}^{-1}$  at 250 m. At the same time, the stratus top rises by 250 m (Figure 13a), resulting in a substantial increase in LWP from  $50 \text{ g}\cdot\text{kg}^{-1}$  to  $240 \text{ g}\cdot\text{kg}^{-1}$ . This increase in water content is mainly due to the advection of cloud mixing ratio (Figure 13c). The peak of cloud advection around 750 m induces a maximum of radiative cooling (Figure 13d), and therefore droplet production by

activation (pink line, Figure 13b), as well as non-negligible turbulent effects on temperature and vapour mixing ratio in the layer. This supply of cloud water above 500 m contributes to the production of cloud water below by advection, under the effect of the subsidence (dashed black line in Figure 13e). Additionally, the water production in the upper part of the cloud induces a significant vertical transport of cloud water below 250 m by droplet sedimentation (dark blue line in Figure 13b). This cloud water supply in the sub-cloud layer mainly evaporates (pink line in Figure 13b), inducing a cooling (Figure 13d) and a moistening (Figure 13e) by the microphysics in the first 450 m, mainly compensating the warm and dry advection at low levels.

For the NE area, advection of LWC over the 800 depth appears as a decisive factor driving the stratus lowering, generating radiative cooling, vertical transport, droplet sedimentation, evaporation, and cooling of the sub-cloud layer.

#### 4.4.2 | OPE subdomain

At OPE, the stratus CTH increases slightly with a lower cloud water content than at NE. During the descent of the

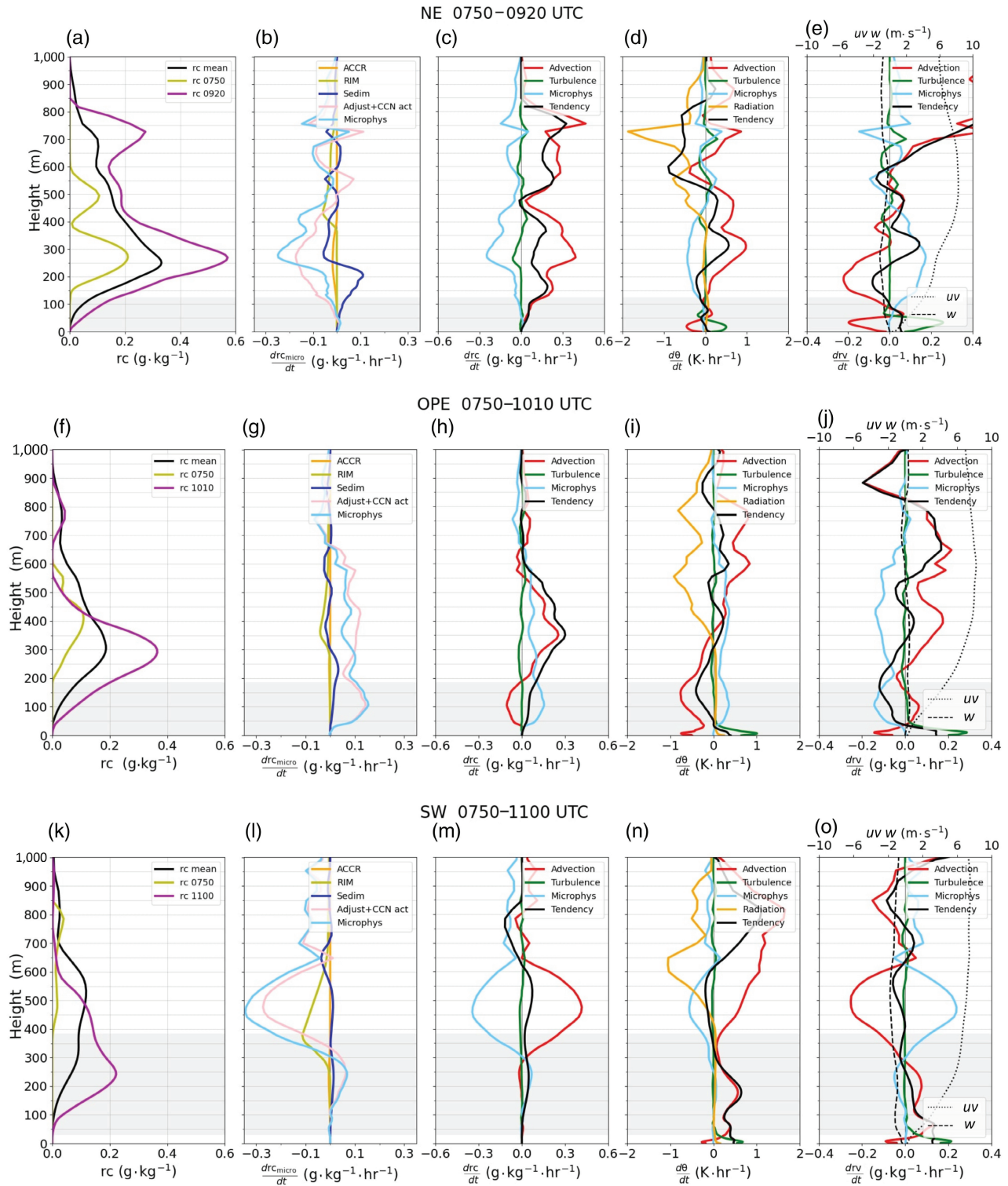


**FIGURE 13** Vertical profiles of: (a, f, k) initial, final (over 5-min periods), and mean cloud mixing ratio; (b, g, l) decomposition of the microphysical terms of the cloud mixing ratio budget (in  $\text{g}\cdot\text{kg}^{-1}\cdot\text{hr}^{-1}$ ), with ACCR the collection processes, RIM the riming, Sedim the droplet sedimentation, Adjust + CCN act the saturation adjustment (condensation/evaporation) and the activation process, and Microphys the total microphysical tendency; (c, h, m) terms of the cloud mixing ratio budget (in  $\text{g}\cdot\text{kg}^{-1}\cdot\text{hr}^{-1}$ ); (d, i, n) terms of the potential temperature budget (in  $\text{K}\cdot\text{hr}^{-1}$ ); (e, j, o) terms of the vapour mixing ratio budget (in  $\text{g}\cdot\text{kg}^{-1}\cdot\text{hr}^{-1}$ ) for the three sites during the stratus lowering period. The first line is NE during 0750–0920 UTC, the second line is OPE during 0750–1010 UTC, and the third line is SW during 0750–1100 UTC. Zonal, meridional, and vertical wind speeds are averaged for the same periods (top axis,  $\text{m}\cdot\text{s}^{-1}$ ) and shown by dotted, dashed, and dot-dashed lines respectively in (e, j, o). For clarity, vertical velocity has been multiplied by 30 [Colour figure can be viewed at [wileyonlinelibrary.com](http://wileyonlinelibrary.com)]

stratus, the maximum LWC increases from  $0.11 \text{ g}\cdot\text{kg}^{-1}$  at 420 m to  $0.38 \text{ g}\cdot\text{kg}^{-1}$  at 300 m. When the stratus reaches the ground at 1010 UTC, the LWP reaches  $132 \text{ g}\cdot\text{m}^{-2}$ , which is four times higher than when it began to lower. However, it does not exceed half of the LWP at NE at the fog formation.

In terms of cloud water budget (Figure 13h), the main difference with the NE subdomain is that the transport of cloud mixing ratio is only a source in the layer between 200 and 550 m, whereas it is almost negligible above and a sink below. Additionally, there is a warm advection above 400 m, which is also present over the other two sites, and this limits the condensation despite the advection of moist air. Without an efficient supply of cloud water in the upper levels, the droplet sedimentation is almost negligible below the stratus (Figure 13g), preventing a cooling and a moistening by evaporation (Figure 13i,j in blue line). However, a positive factor for the stratus lowering is an advection of cold air in the first 300 m, favouring condensation and the extension of the stratus towards the ground. The origin of this cold advection will be discussed further in Section 6. Near the ground, this cold advection mainly compensates the warming by turbulent heat flux (green line in Figure 13i). Indeed, the positive contribution of turbulence in the potential temperature budget in the first 50 m is due to the solar heating artificially induced by the time lag. But this is small compared with the cooling caused by the advection in the first 400 m, and it does not prevent the fog formation. Hence, the stratus lowers at OPE despite the absence of cloud water supply in the upper part of the stratus, and it succeeds in reaching the ground due mainly to a cold air advection in the lower levels.

#### 4.4.3 | SW subdomain

At SW, the stratus begins to lower at the same time as the other sites but with a much lower LWP ( $10 \text{ g}\cdot\text{m}^{-2}$ ) and a higher cloud base around 380 m (Figure 13k). More than 3 hr later, the cloud base has decreased to 30 m above the ground with a maximum of cloud water content ( $0.22 \text{ g}\cdot\text{kg}^{-1}$ ), which is located at 250 m. After, the base remains constant and then goes up. At the same time, the top of the stratus did not rise. The budgets show that there is a significant supply of cloud water by advection between 300 and 650 m, largely evaporated by an advection of warm and dry air. The riming process also contributes to consume supercooled cloud water more than at the other sites. In the same way as in OPE, there is no source of cloud water by advection in the upper part of the stratus above 650 m to feed the droplet sedimentation downwards (Figure 13l). Below 300 m there is a warm advection, unlike the OPE area, acting against the condensation up to the ground despite the moistening by transport. The

solar heating due to the time lag adds to the warmer advection to prevent stratus from collapsing to the ground, but the turbulent contribution in the first 50 m is not higher than at the other sites and, therefore, is not decisive for the non-formation of fog.

We can also note that, between the three sites, the subsidence is higher at SW; this means that the subsidence is not a major ingredient for the continental stratus lowering if the supply of cloud water in the stratus layer is not sufficient. Hence, the main reason why the fog does not form at SW compared with the other sites is that the transport brings neither cloud water above the stratus compared with NE, nor cold air in the sub-cloud layer compared with OPE.

To summarize, the advection of cloud water in the stratus appears crucial through its impact on the top cloud radiative cooling, which stimulates activation of cloud droplets and mixing, favouring vertical transport of liquid water under the effect of subsidence and sedimentation. If this supply of cloud water is not sufficient for the stratus to reach the ground, advection of cold air in the sub-cloud layer can help to complete the lowering. In any case, non-local processes drive the stratus lowering during this event.

The next section will focus on microphysical processes through different sensitivity tests.

## 5 | MICROPHYSICAL SENSITIVITY TESTS

The previous section has shown the primary role of non-local processes. In a second step, the objective is to analyse the impact of microphysical processes, considering the same dynamical conditions. Therefore, we focus on the OPE site and conduct sensitivity tests on the microphysics.

In the first part, two simulations with the one-moment microphysical scheme ICE3 imposing two different droplet concentrations are compared with the observations and with the LIMA simulation at the OPE station. In the second part, sensitivity tests are conducted with the LIMA scheme in order to characterize the role of droplet settling and raindrop evaporative cooling. Except for the microphysics and cloud optical properties computation for the radiation scheme with ICE3, the configuration is the same as in the reference simulation.

### 5.1 | One-moment versus two-moment microphysical schemes

Two simulations are performed with ICE3 using constant droplet NCs of  $300 \text{ cm}^{-3}$  (ICE3-300) and  $100 \text{ cm}^{-3}$

(ICE3-100). These values correspond to the constant droplet concentrations used in the operational configuration of AROME for continental and maritime areas respectively. They also fall within the range of the observed droplet concentrations (Figure 9b,d). However, none of these values match perfectly the observed values for either the stratus or the fog due to the substantial variability of droplet concentration within the clouds:  $N_c = 300 \text{ cm}^{-3}$  better matches the observation within the stratus before the lowering but overestimates it near the stratus base and in the fog layer, in contrast to LIMA, whereas  $N_c = 100 \text{ cm}^{-3}$  matches almost exactly the observation in the upper part of the fog but underestimates the values near the ground and in the stratus before the lowering.

Independently of the microphysical scheme, the stratus forms at the same time as in the LIMA simulation, around 2300 UTC, which is mainly due to the large-scale conditions of the AROME analyses forcing Meso-NH, and the cloud base descends rapidly much lower than in the observations (Figure 8c). Up to 0200 UTC, the evolutions of LWC and LWP (Figure 7a in blue line) are very close between both simulations. Between 0230 and 0400 UTC, ICE3-300 produces a lower stratus base height than LIMA and the observations, with higher values of LWC throughout the cloud layer. Consequently, the LWP is even more overestimated with ICE3-300 than LIMA. Indeed, LIMA produces droplet concentrations higher than  $300 \text{ cm}^{-3}$  during this period. For the same cloud water content, droplets are then bigger in ICE3-300, favouring sedimentation, cooling by evaporation below the stratus, and a faster lowering. However, the cloud does not reach the ground in ICE3-300 due to the large-scale drying conditions between 0400 and 0630 UTC. At the end of this dry period, the cloud water content is much reduced with ICE3-300, leading to lower values of the LWP and LWD (Figure 7b). When the stratus is reforming again after 0700 UTC, it lowers faster than in LIMA and the observations, but the fog onset occurs only 20 min earlier in ICE3-300 than in LIMA. The shapes of the LWC profiles are also very similar in the two simulations (Figure 9a,c). The accumulated water at the ground as a result of the sedimentation of cloud droplets and raindrops is also equivalent, with around 0.003 mm for the cloud water and 0.5 mm for the rainwater at OPE up to 1400 UTC (not shown). Therefore, ICE3-300 and LIMA simulations are very close to each other for this STL case.

Although the general stratus life cycle is the same, the ICE3-100 simulation displays a different behaviour, with an earlier fog formation at 0330 UTC. After a temporary dissipation around 0525 UTC due to the large-scale drying, a new fog forms again at 0710 UTC, following a very rapid stratus lowering, and persists for a long time, up to

1230 UTC, which is the same dissipation time for all the simulations. Hence, ICE3-100 does not correctly simulate the STL as fog formation is anticipated by 6.5 hr, compared with the observations (considering the time lag), due to the lower droplet NC.

Although the STL is different between ICE3-100 and the other simulations and the observation, the differences in the LWP and LWD evolutions are smaller (Figure 7). But during the dry period between 0430 and 0700 UTC, both ICE3 simulations produce lower values of LWP than LIMA does, and the almost total dissipation of the cloud between 0600 and 0700 UTC with a strong underestimation of LWD compared with the observations. Given that LIMA produces values of droplet concentration larger than  $300 \text{ cm}^{-3}$ , one could argue that in both ICE3 simulations the droplet evaporation during the drier period is enhanced due to an excess of droplet sedimentation. We can note that the shapes of the LWC profiles with ICE3-100 are similar to the other simulations during the stratus and fog periods (Figure 9a,c), meaning that the earlier fog formation does not modify radically its characteristics in terms of vertical structure and LWP.

To better illustrate the processes, the influence of the microphysics on the STL is presented at OPE in terms of differences between ICE3-100 and LIMA for the LWC (Figure 14a), the sedimentation contribution to the cloud mixing ratio budget (Figure 14b), the microphysical contribution to the potential temperature budget (Figure 14c), and the vapour mixing ratio budget (Figure 14d).

In the upper part of the stratus, ICE3-100 loses water through sedimentation, which induces the growth of droplets by coalescence. The bigger droplets fall below the stratus, favouring cooling and moistening beneath the stratus by evaporation. When the sub-cloud layer reaches saturation, cloud droplets can no longer evaporate and continue to fall, leading to the fog formation. Accumulated cloud water at the ground during the whole event over the domain is almost 10 times higher with ICE3-100 than with LIMA, whereas accumulated rainwater is almost unchanged (not shown). Hence, droplet sedimentation is of major importance to accelerate the stratus lowering. A low value of droplet concentration induces larger droplet diameters, favouring droplet settling. Therefore, the choice of the NC for one-moment microphysical schemes has a strong impact on the stratus lowering and fog formation time prediction. On the contrary, it does not impact significantly the LWP evolution during the whole event and the fog characteristics in terms of LWC profiles. Considering the variability of the observed droplet concentration within the stratus and the fog, a constant value cannot be representative of the range of concentrations, and a two-moment microphysical scheme seems more appropriate.

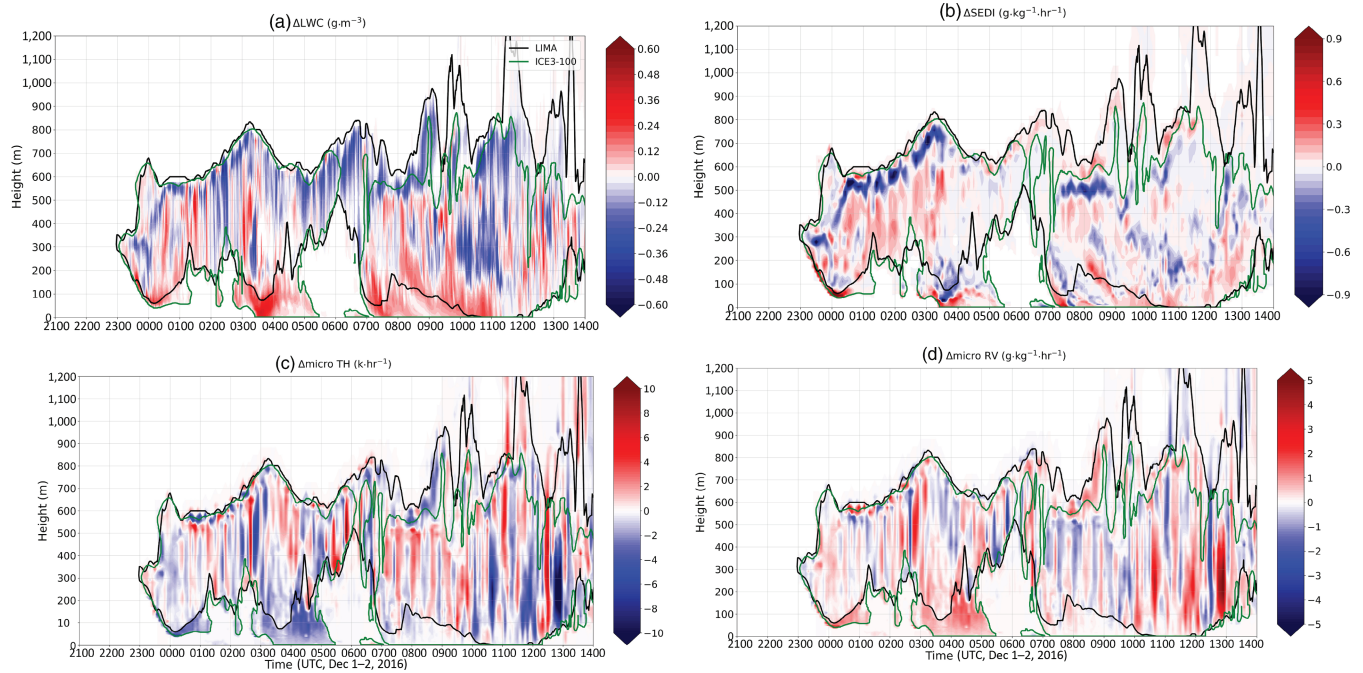


**FIGURE 14** Temporal evolution at OPE of vertical profiles of the difference between ICE3-100 and LIMA of (a)  $\Delta\text{LWC}$  ( $\text{g}\cdot\text{m}^{-3}$ ), (b) sedimentation contribution to the cloud mixing ratio budget  $\Delta\text{SEDI}$  ( $\text{g}\cdot\text{kg}^{-1}\cdot\text{hr}^{-1}$ ), (c) microphysical contribution to the potential temperature budget  $\Delta\text{micro TH}$  ( $\text{K}\cdot\text{hr}^{-1}$ ), and (d) microphysical contribution to the vapour mixing ratio budget  $\Delta\text{micro RV}$  ( $\text{g}\cdot\text{kg}^{-1}\cdot\text{hr}^{-1}$ ). The cloud contours (in black for LIMA and green for ICE3-100) are given by the  $10^{-2}$   $\text{g}\cdot\text{m}^{-3}$  LWC threshold [Colour figure can be viewed at [wileyonlinelibrary.com](http://wileyonlinelibrary.com)]

## 5.2 | Impact of droplet sedimentation and raindrop evaporative cooling

We now focus on the two-moment microphysical scheme LIMA in order to better characterize the microphysical processes impacting the STL. The NOSED simulation presents the same configuration as LIMA except that the droplet sedimentation is switched off. Since NOSED will tend to produce more rainwater, it might be wise to see if evaporative cooling of rain has an impact on stratus lowering and fog formation. The second simulation NOSED + NOCOOL switches off the rain evaporative cooling in addition to the cloud droplet sedimentation.

The stratus life cycle at the OPE site for NOSED and NOSED + NOCOOL, presented in Figure A1, is almost similar to the LIMA simulation, confirming that it is mainly driven by non-local conditions. The differences appear near the ground, where the fog formation is slightly delayed with NOSED and does not occur in NOSED + NOCOOL. This is consistent with the results obtained with the ICE3 simulation, where the settling of cloud droplets leads to moistening and cooling in the sub-cloud layer. The absence of sedimentation tends to increase slightly the raindrop formation, so the absence of

cooling by raindrop evaporation prevents the fog formation at OPE. Other small differences appear between LIMA and NOSED simulations: NOSED maintains a slightly higher cloud top in addition to the higher cloud base, especially during the dry period between 0400 and 0630 UTC, as the cloud water remains at higher levels. Additionally, a reduction of LWC is noted with NOSED during the stratus life cycle, due to formation of snow (not shown) in addition to rain, by consuming supercooled droplets.

The effect of disallowing the sedimentation processes is also seen to increase slightly the NC. This is hypothesized to be due to a reduction of droplet coalescence, which predominately occurs when droplets fall through the cloud, causing larger droplets to be produced. For a constant LWC, a reduction in the average droplet diameter will result in a higher NC. This explains why, despite the reduction in LWC seen with NOSED, a slight increase in the NC is observed.

For the NOSED + NOCOOL configuration, stopping the evaporative cooling of raindrops induces warmer air below the cloud layer. This decreases the CCN activation and the formation of droplets, reducing the droplet concentration in NOSED + NOCOOL compared with NOSED (Figure A1b,d).

The impact of droplet sedimentation on the fog formation is confirmed over the whole domain, as presented in Figure 10c,d with the fog onset time. Only 47% of the domain in NOSED and 43% in NOSED + NOCOOL is affected by fog formation, compared with 75% with LIMA. Without droplet sedimentation, fog is limited to the area where cold air is advected in the first 250 m (not shown).

NOSED + NOCOOL has a relatively similar behaviour to NOSED, underlining the fact that the main contribution to the cooling below the stratus is produced by the evaporation of droplets more than raindrops. Note that the cumulated ground precipitation rate over the domain is slightly increased from LIMA to NOSED, and slightly reduced from NOSED to NOSED + NOCOOL (not shown), as the absence of cooling from raindrop evaporation warms the sub-cloud layer and increases the evaporation of raindrops before reaching the ground.

To summarize, the absence of droplet sedimentation and cooling by raindrop evaporation strongly limits the fog formation by STL, but does not prevent it where non-local conditions are the most favourable.

## 6 | DISCUSSION

Vertical profiles of LWC and droplet NC derived from in-situ measurements under the tethered balloon exhibited different shapes between the stratus and the fog formed below, and a significant variability. Lower values of LWC and droplet NC in fog than in clouds are commonly observed (Pearson *et al.*, 2009; Price, 2011; Mazoyer *et al.*, 2019). This could be explained by lower supersaturation values reached in fog due to the lack of significant updraughts in stable boundary layers. It has led to simple alterations to single-moment schemes being implemented in operational settings to taper the drop number towards the ground (Wilkinson *et al.*, 2013; Boutle *et al.*, 2018). However, measurements reported here reveal that both LWC and droplet NC decrease drastically in the upper part of the fog layer. This shape is singular and requires additional analysis that will be presented in a forthcoming paper.

This study has presented the first high-resolution simulation for a real case of continental fog formed by stratus lowering. Contrary to previous studies that have shown the importance of large-scale subsidence for STL fog over sea (e.g., Koracin *et al.*, 2001), it is not shown here that this plays a primary role in fog formation over land. The analysis, based on cloud mixing ratio and potential temperature budgets, reveals that three-dimensional advection processes are crucial to feed the stratus and to favour the stratus base lowering and form the fog, without being restricted to large-scale vertical velocity.

Three-dimensional non-local processes are also well identified in observations, where the layer between 550 and 1400 m exhibited a significant cooling and moistening during the stratus life cycle.

Other criteria, such as the CBH, are often identified as key parameters indicative of fog formation in a stratus lowering. From a statistical analysis of 64 stratus lowering events, Dupont *et al.* (2016) found that STL leading to fog has an average cloud base of  $172 \pm 120$  m during the 3 hr period before fog formation, whereas quasi-fog situations (visibility between 1 and 2 km) correspond to more elevated stratus (average CBH of  $804 \pm 225$  m). In addition the CBH subsidence rate is much lower for the fog events ( $44 \text{ m}\cdot\text{hr}^{-1}$ ) than for the quasi-fog situations ( $280 \text{ m}\cdot\text{hr}^{-1}$ ). In our case study, measurements of CBH from the ceilometer for both lowering events are sufficiently low (240 m at 2100 UTC and 120 m at 0300 UTC in the reference time of the observation), as well as the CBH subsidence rate ( $63 \text{ m}\cdot\text{hr}^{-1}$  and  $40 \text{ m}\cdot\text{hr}^{-1}$  respectively), but only the second lowering event led to fog formation. For the first case, the advection of warm and dry air in the sub-cloud layer has prevented the lowering of the stratus cloud base to the surface. Measurements with the tethered balloon confirm that the initial stratus layer has gradually disappeared, associated with a significant increase in air temperature. Beyond the CBH consideration, this means that the analysis cannot be conducted in a one-dimensional approach.

In the same way, the CTH, which could be considered as a good tracer of the moist air supply in the upper part of the stratus feeding the stratus lowering, is not sufficient to predict fog formation in STL as warmer or drier air in the sub-cloud layer, such as around SW, has stopped the lowering (Figure 12a).

The conceptual model proposed by Toledo *et al.* (2021) explains the fog formation by STL when the LWP exceeds the critical value corresponding to the sufficient amount of fog liquid water to extend all the way down to the surface. The reservoir LWP, defined as the excess water with respect to the critical value (Toledo *et al.*, 2021, equation 5), is always negative between 2300 and 1200 UTC over the whole domain of simulation, even when the fog forms (not shown). A reason could be that the CTH in our case is between 600 and 900 m while Toledo *et al.* (2021) have defined a maximum value of 462 m derived from their 56 fog events. This results in very high values of the CLWP, always larger than  $300 \text{ g}\cdot\text{m}^{-2}$ , while the simulated and the observed LWP never exceed  $250 \text{ g}\cdot\text{m}^{-2}$ . In addition, the stratus that forms the fog and the resulting fog itself (Figure 8a,b) are largely sub-adiabatic (the dilution ratio is equal to 0.4), whereas it is a main hypothesis for the validity of the conceptual model. Despite these considerations, if we disregard the formulation itself and consider only the concept with an NLWP to represent the layer between

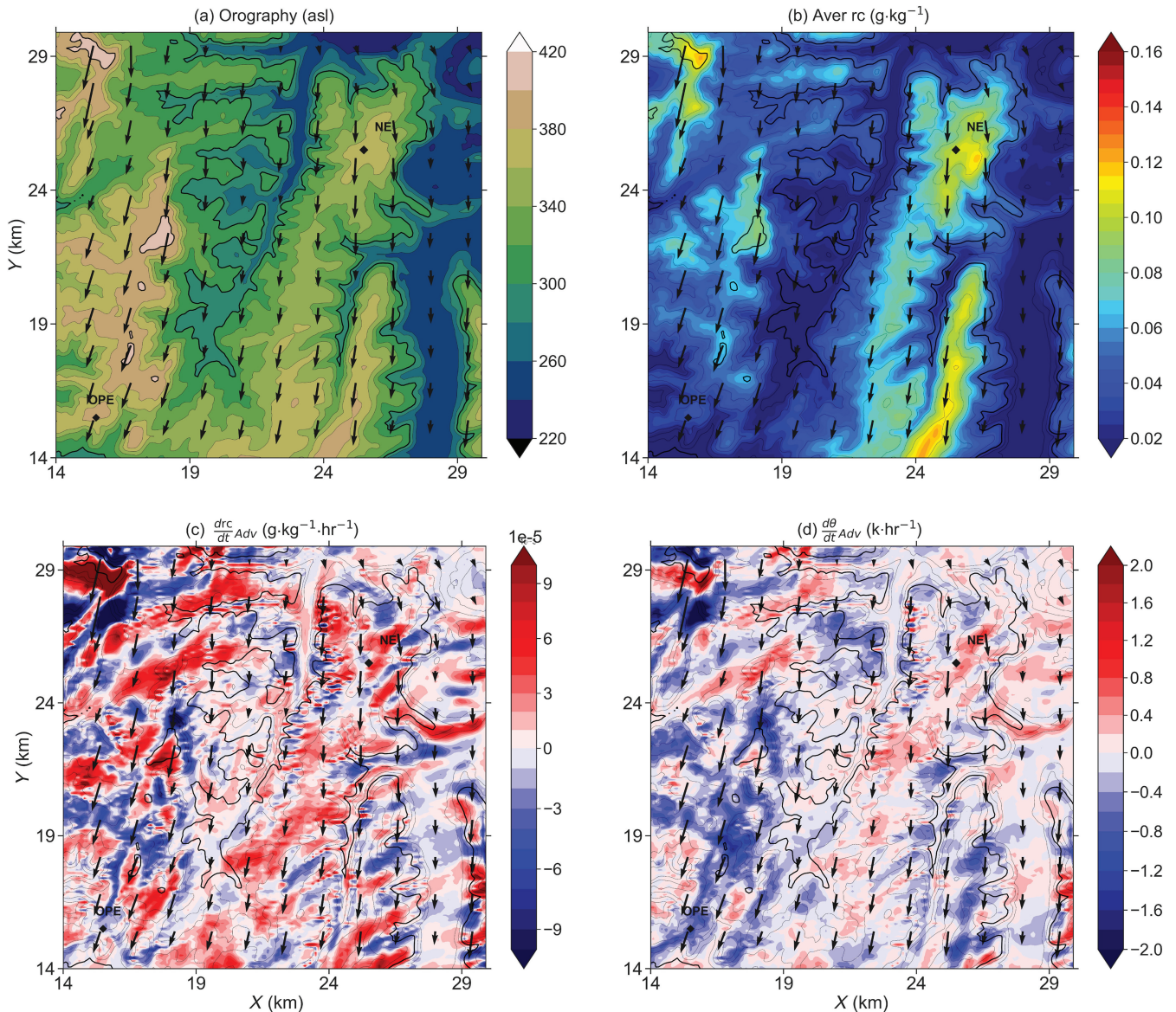


**FIGURE 15** Zoom on the northeast quarter of the domain of (a) the orography, (b) the mean cloud mixing ratio (in  $\text{g}\cdot\text{kg}^{-1}$ ), (c) the advective term of cloud mixing ratio tendency (in  $\text{g}\cdot\text{kg}^{-1}\cdot\text{h}^{-1}$ ), and (d) the advective term of potential temperature tendency (in  $\text{K}\cdot\text{h}^{-1}$ ), in the first 250 m layer above the ground between 0750 and 1010 UTC, with the arrows of the mean horizontal wind and the contour line at 300 m superimposed [Colour figure can be viewed at [wileyonlinelibrary.com](http://wileyonlinelibrary.com)]

the ground and the CTH to be filled by the cloud water, Figure 12b has shown that fog formation is not always correlated with a strong value of NLWP, and strong values of NLWP do not always lead to fog. This means that the conceptual model, developed in a one-dimensional framework, cannot be generalized to fog by STL and a three-dimensional model is necessary to make an accurate fog forecast.

The role of droplet sedimentation was found to be a driving process for the stratus lowering by moistening the sub-cloud layer through evaporation in Dupont *et al.* (2012). This process is also well identified in our study using the microphysical budget analysis, but it appears as

a consequence of the advection of cloudy, cold and humid air, and not as the triggering factor. Hence, at the SW location, cloud advection between 300 and 600 m is significant, but the simultaneous advection of warm air in the same layer favours evaporation and prevents the sedimentation of droplets below. In the same way, the fall of the stratus at OPE around 0000 and 0330 UTC, initiated by the arrival of cloudy air, is stopped by the advection of warm and dry air. Moreover, a test without sedimentation and raindrop evaporative cooling limits the fog formation but does not prevent the stratus lowering; the fog still forms in some areas where the cold air is advected to. It is the coupling between both non-local and local phenomena, therefore,

that allows the base of the stratus to lower and form the fog.

Considering the non-local effects, the budget analysis conducted over the NE, OPE, and SW sites has shown that the cloud water advection in the stratus was systematically present to feed the stratus lowering. But advective contributions were much more different between the three sites in the first 250 m layer, with a positive contribution to cloud water tendency at NE and a negative one at OPE, whereas the advection brought cold air at OPE and warm air at SW. To better understand this variability in the low levels, Figure 15 presents a zoom on the northeast quarter of the domain of the mean cloud mixing ratio and advective terms of cloud mixing ratio and potential temperature in the first 250 m layer between 0750 and 1010 UTC. Advective terms of cloud mixing ratio and potential temperature (Figure 15c,d) present fine-scale structures correlated with the orography (Figure 15a) when clouds are already present in the layer (Figure 15b). In a north to northeast flow, the advective contribution to cloud water tends to be positive on the top of the hills and negative in the valleys, whereas the advective contribution to potential temperature tends to be positive on the windward slopes of the hills and negative on the downwind sides. Thus, even if the cloud advection that drives the stratus lowering concerns the whole domain, affecting the northeast area first, non-local fine-scale effects mainly induced by the orography modulate the formation or not of fog. This underlines the importance of high-resolution simulation to correctly simulate fog by STL over hilly terrains, as Ducongé *et al.* (2020) already pointed out for radiation fog.

## 7 | CONCLUSION

A case study of fog formed by stratus lowering that was observed during a field experiment on the night of December 1–2, 2016, has been presented.

A three-dimensional numerical simulation of this case has been performed with the Meso-NH model applied at 100 m grid spacing with a downscaling approach from the AROME analyses focusing on the stratus lowering and the fog formation. It has been first validated with the thermodynamical and microphysical measurements. Despite the 4 hr delay of the stratus formation time, which was due to large-scale conditions, the reference simulation, using the two-moment microphysical scheme LIMA, reproduced correctly the main features of the three phases of the cloud event, allowing it to be used as a basis for analysis.

The stratus lowering over three subdomains has been investigated using a budget analysis of cloud mixing ratio

and potential temperature to better understand the processes involved. Key factors affecting the stratus lowering up to the fog formation include, first, non-local effects, inducing local processes: the advection of cloud water in the upper part of the stratus through its impact on the cloud top radiative cooling, which stimulates activation of cloud droplets and mixing, favouring vertical transport of liquid water under the effect of subsidence and sedimentation. The droplets fall to and beyond the cloud base, which cools and moistens the sub-cloud layer by evaporation.

Other non-local fine-scale effects, as a consequence of orographic circulations in the first 250 m, come to modulate the stratus lowering by accelerating or preventing the fog formation. The stratus descent tends to be accelerated on the windward slopes and at the top of the hills and slowed down on the leeward sides. In the same way, these circulations feed the droplet sedimentation, evaporation, and cooling of the sub-cloud layer. Hence, the non-local effects appear to be the trigger component of the local effects favouring the stratus lowering and the fog formation, which are the droplet sedimentation, the evaporation, and the cooling in the sub-cloud layer. Therefore, a conceptual model based on a CLWP in a one-dimensional framework cannot be generalized to fog by STL, and a three-dimensional high-resolution model is necessary to make an accurate fog forecast.

The study has also shown that accurate prediction of cloud droplet NC is one factor important in correctly forecasting the onset of fog by stratus lowering. A too low NC leads to droplets that are too big and sediment out too fast, quickly leading to fog formation, and vice-versa. To address this issue, a two-moment microphysical scheme appears more appropriate than a one-moment scheme in light of the droplet concentration variability. In the same way, taking into account the settling of cloud droplets is crucial to correctly predict fog by stratus lowering.

Although this study dealt with only one case study, it had the interest of containing different scenarios of stratus lowering leading or not to fog, depending on the location or the period considered. It will, of course, be useful to study other cases in depth to confirm the triggering factor of non-local effects and then the coupling between non-local and local processes in the stratus lowering.

Increased observations could, therefore, help to better characterize the processes in a three-dimensional approach, as in the LANFEX (Price *et al.*, 2018) or SOFOG3D experimental campaigns but which did not include cases of fog by stratus lowering. W-band Doppler cloud radars, measuring three-dimensional reflectivity and Doppler velocity along sight of water drops, are ideal tools to provide simultaneously dynamical and microphysical information (Delanoë *et al.*, 2016). Techniques

are also being developed on multi-instrumental retrievals of cloud properties (Bell *et al.*, 2021) that could allow continuous measurement of vertical profiles of liquid water content and droplet concentration inside stratus clouds. This would further aid the study of stratus-lowering fog.

## AUTHOR CONTRIBUTIONS

**Maroua Fathalli:** Conceptualization; data curation; formal analysis; investigation; methodology; software; validation; visualization; writing—original draft; writing—review and editing. **Christine Lac:** Conceptualization; investigation; methodology; supervision; writing—original draft; writing—review and editing. **Frédéric Burnet:** Conceptualization; investigation; methodology; supervision; writing—original draft; writing—review and editing. **Benoît Vié:** Software; validation; investigation.

## ACKNOWLEDGEMENTS

The fog campaign was conducted by CNRM in collaboration with IRSN (Institut de Radioprotection et de Sûreté Nucléaire). We would like to acknowledge Sebastien Conil from ANDRA for providing access to the atmospheric platform and aerosol measurements used in this study, and Emmanuel Fontaine and colleagues from CNRM/CEMS for the satellite products. We are grateful to the CNRM/G-MEI team for the instrumentation deployment, the tethered balloon operations, and the data processing. Moreover, we acknowledge the contribution of all the participants involved in the field campaign. Finally, we thank Marie Mazoyer for fruitful discussions during this study.

## ORCID

M. Fathalli  <https://orcid.org/0000-0002-7832-4297>

C. Lac  <https://orcid.org/0000-0003-0324-3991>

F. Burnet  <https://orcid.org/0000-0003-0572-4422>

## REFERENCES

- American Meteorological Society (2017). Fog. *Glossary of Meteorology*. <https://glossary.ametsoc.org/wiki/Fog>.
- Bell, A., Martinet, P., Caumont, O., Vié, B., Delanoé, J., Dupont, J.-C. and Borderies, M. (2021) W-band radar observations for fog forecast improvement: An analysis of model and forward operator errors. *Atmospheric Measurement Techniques*, 14(7), 4929–4946.
- Bergot, T. (2016) Large-eddy simulation study of the dissipation of radiation fog. *Quarterly Journal of the Royal Meteorological Society*, 142(695), 1029–1040.
- Bergot, T., Escobar, J. and Masson, V. (2015) Effect of small-scale surface heterogeneities and buildings on radiation fog: Large-eddy simulation study at Paris–Charles de Gaulle Airport. *Quarterly Journal of the Royal Meteorological Society*, 141(686), 285–298.
- Berry, E.X. and Reinhardt, R.L. (1974) An analysis of cloud drop growth by collection: Part II. Single initial distributions. *Journal of the Atmospheric Sciences*, 31, 1825–1831.
- Bougeault, P. and Lacarrere, P. (1989) Parameterization of orography-induced turbulence in a mesobeta-scale model. *Monthly Weather Review*, 117(8), 1872–1890.
- Boutle, I., Angevine, W., Bao, J.-W., Bergot, T., Bhattacharya, R., Bott, A., Ducongé, L., Forbes, R., Goecke, T., Grell, E., Hill, A., Igel, A.L., Kudzotsa, I., Lac, C., Maronga, B., Romakkaniemi, S., Schmidli, J., Schwenkel, J., Steeneveld, G.-J. and Vié, B. (2022) Demistify: A large-eddy simulation (LES) and single-column model (SCM) intercomparison of radiation fog. *Atmospheric Chemistry and Physics*, 22(1), 319–333.
- Boutle, I., Eyre, J. and Lock, A. (2014) Seamless stratocumulus simulation across the turbulent gray zone. *Monthly Weather Review*, 142(4), 1655–1668.
- Boutle, I., Price, J., Kudzotsa, I., Kokkola, H. and Romakkaniemi, S. (2018) Aerosol–fog interaction and the transition to well-mixed radiation fog. *Atmospheric Chemistry and Physics*, 18(11), 7827–7840.
- Brousseau, P., Seity, Y., Ricard, D. and Léger, J. (2016) Improvement of the forecast of convective activity from the AROME-France system. *Quarterly Journal of the Royal Meteorological Society*, 142(699), 2231–2243.
- Canut, G., Couvreur, F., Lothon, M., Legain, D., Pignatelli, B., Lampert, A., Maurel, W. and Moulin, E. (2016) Turbulence fluxes and variances measured with a sonic anemometer mounted on a tethered balloon. *Atmospheric Measurement Techniques*, 9(9), 4375–4386.
- Cohard, J.-M. and Pinty, J.-P. (2000) A comprehensive two-moment warm microphysical bulk scheme. I: Description and tests. *Quarterly Journal of the Royal Meteorological Society*, 126(566), 1815–1842.
- Cohard, J.-M., Pinty, J.-P. and Bedos, C. (1998) Extending Twomey's analytical estimate of nucleated cloud droplet concentrations from CCN spectra. *Journal of the Atmospheric Sciences*, 55(22), 3348–3357.
- Colella, P. and Woodward, P.R. (1984) The piecewise parabolic method (PPM) for gas-dynamical simulations. *Journal of Computational Physics*, 54(1), 174–201.
- Conil, S., Helle, J., Langrene, L., Laurent, O., Delmotte, M. and Ramonet, M. (2019) Continuous atmospheric CO<sub>2</sub>, CH<sub>4</sub> and CO measurements at the Observatoire Pérenne de l'Environnement (OPE) station in France from 2011 to 2018. *Atmospheric Measurement Techniques*, 12(12), 6361–6383.
- Cuxart, J. (2015) When can a high-resolution simulation over complex terrain be called LES?. *Frontiers in Earth Science*, 3, 87.
- Cuxart, J., Bougeault, P. and Redelsperger, J.-L. (2000) A turbulence scheme allowing for mesoscale and large-eddy simulations. *Quarterly Journal of the Royal Meteorological Society*, 126(562), 1–30.
- Deardorff, J.W. (1980) Stratocumulus-capped mixed layers derived from a three-dimensional model. *Boundary-Layer Meteorology*, 18(4), 495–527.
- Delanoé, J., Protat, A., Vinson, J.-P., Brett, W., Caudoux, C., Bertrand, F., Parent du Châtelet, J., Hallali, R., Barthes, L., Haeffelin, M. and Dupont, J.C. (2016) BASTA: A 95-GHz FMCW Doppler radar for cloud and fog studies. *Journal of Atmospheric and Oceanic Technology*, 33(5), 1023–1038.
- Ducongé, L., Lac, C., Vié, B., Bergot, T. and Price, J. (2020) Fog in heterogeneous environments: The relative importance of local

- and non-local processes on radiative-advective fog formation. *Quarterly Journal of the Royal Meteorological Society*, 146(731), 2522–2546.
- Dupont, J., Haeffelin, M., Stolaki, S. and Elias, T. (2016) Analysis of dynamical and thermal processes driving fog and quasi-fog life cycles using the 2010–2013 ParisFog dataset. *Pure and Applied Geophysics*, 173(4), 1337–1358.
- Dupont, J.-C., Haeffelin, M., Protat, A., Bouniol, D., Boyouk, N. and Morille, Y. (2012) Stratus-fog formation and dissipation: A 6-day case study. *Boundary-Layer Meteorology*, 143(1), 207–225.
- Farah, A., Villani, P., Rose, C., Conil, S., Langrene, L., Laj, P. and Sellegri, K. (2020) Characterization of aerosol physical and optical properties at the Observatoire Pérenne de l'Environnement (OPE) site. *Atmosphere*, 11(2), 172.
- Fernando, H.J., Gultepe, I., Dorman, C., Pardyjak, E., Wang, Q., Hoch, S., Richter, D., Creegan, E., Gaberšek, S., Bullock, T., Hocut, C., Chang, R., Alappattu, D., Dimitrova, R., Flagg, D., Grachev, A., Krishnamurthy, R., Singh, D.K., Lozovatsky, I., Nagare, B., Sharma, A., Wagh, S., Wainwright, C., Wroblewski, M., Yamaguchi, R., Bardoel, S., Coppersmith, R.S., Chisholm, N., Gonzalez, E., Gunawardena, N., O.Hyde, Morrison, T., Olson, A., Perelet, A., Perrie, W., Wang, S. and Wauer, B. (2021) C-FOG: Life of coastal fog. *Bulletin of the American Meteorological Society*, 102(2), E244–E272.
- Fouquart, Y. and Bonnel, B. (1980) Computations of solar heating of the Earth's atmosphere: A new parameterization. *Beiträge zur Physik der Atmosphäre*, 53(1), 35–62.
- Gultepe, I., Sharman, R., Williams, P.D., Zhou, B., Ellrod, G., Minnis, P., Trier, S., Griffin, S., Yum, S.S., Gharabaghi, B., Feltz, W., Temimi, M., Pu, Z., Storer, L.N., Kneringer, P., Weston, M.J., Chuang, H.-Y., Thobois, L., Dimri, A.P., Dietz, S.J., França, G.B., Almeida, M.V. and Albuquerque Neto, F.L. (2019) A review of high impact weather for aviation meteorology. *Pure and Applied Geophysics*, 176(5), 1869–1921.
- Haeffelin, M., Bergot, T., Elias, T., Tardif, R., Carrer, D., Chazette, P., Colomb, M., Drobinski, P., Dupont, E., Dupont, J.-C., Gomes, L., Musson-Genon, L., Pietras, C., Plana-Fattori, A., Protat, A., Rangognio, J., Raut, J.-C., Rémy, S., Richard, D., Sciare, J. and Zhang, X. (2010) PARISFOG: Shedding new light on fog physical processes. *Bulletin of the American Meteorological Society*, 91(6), 767–783.
- Kessler, E. (1969) *On the distribution and continuity of water substance in atmospheric circulations*, Meteorological Monographs Vol. 10. Boston, MA: American Meteorological Society.
- Koracin, D., Lewis, J., Thompson, W.T., Dorman, C.E. and Businger, J.A. (2001) Transition of stratus into fog along the California coast: Observations and modeling. *Journal of the Atmospheric Sciences*, 58(13), 1714–1731.
- Lac, C., Chaboureaud, P., Masson, V., Pinty, P., Tulet, P., Escobar, J., Leriche, M., Barthe, C., Aouizerats, B., Augros, C., Aumond, P., Auguste, F., Bechtold, P., Berthet, S., Bielli, S., Bosseur, F., Caumont, O., Cohard, J.-M., Colin, J., Couvreux, F., Cuxart, J., Delautier, G., Dauhut, T., Ducrocq, V., Filippi, J.-B., Gazen, D., Geoffroy, O., Gheusi, F., Honnert, R., Lafore, J.-P., Lebeaupin Brossier, C., Libois, Q., Lunet, T., Mari, C., Maric, T., Mascart, P., Mogé, M., Molinié, G., Nuissier, O., Pantillon, F., Peyrillé, P., Pergaud, J., Perraud, E., Pianezze, J., Redelsperger, J.-L., Ricard, D., Richard, E., Riette, S., Rodier, Q., Schoetter, R., Seyfried, L., Stein, J., Suhre, K., Taufour, M., Thouron, O., Turner, S., Verrelle, A., Vié, B., Visentin, F., Vionnet, V. and Wautelet, P. (2018) Overview of the Meso-NH model version 5.4 and its applications. *Geoscientific Model Development*, 11, 1929–1969.
- Martin, G., Johnson, D. and Spice, A. (1994) The measurement and parameterization of effective radius of droplets in warm stratocumulus clouds. *Journal of Atmospheric Sciences*, 51(13), 1823–1842.
- Martinet, P., Cimini, D., Burnet, F., Ménétrier, B., Michel, Y. and Unger, V. (2020) Improvement of numerical weather prediction model analysis during fog conditions through the assimilation of ground-based microwave radiometer observations: A 1D-var study. *Atmospheric Measurement Techniques*, 13(12), 6593–6611.
- Masson, V., Le Moigne, P., Martin, E., Faroux, S., Alias, A., Alkama, R., Belamari, S., Barbu, A., Boone, A. and Bouysse, F. (2013) The SURFEXv7.2 land and ocean surface platform for coupled or offline simulation of Earth surface variables and fluxes. *Geoscientific Model Development*, 6, 929–960. et al.
- Mazoyer, M., Burnet, F., Denjean, C., Roberts, G.C., Haeffelin, M., Dupont, J.-C. and Elias, T. (2019) Experimental study of the aerosol impact on fog microphysics. *Atmospheric Chemistry and Physics*, 19(7), 4323–4344.
- Mlawer, E.J., Taubman, S.J., Brown, P.D., Iacono, M.J. and Clough, S.A. (1997) Radiative transfer for inhomogeneous atmospheres: RRTM, a validated correlated-k model for the longwave. *Journal of Geophysical Research: Atmospheres*, 102(D14), 16663–16682.
- Noilhan, J. and Planton, S. (1989) A simple parameterization of land surface processes for meteorological models. *Monthly Weather Review*, 117(3), 536–549.
- Oliver, D., Lewellen, W. and Williamson, G. (1978) The interaction between turbulent and radiative transport in the development of fog and low-level stratus. *Journal of the Atmospheric Sciences*, 35(2), 301–316.
- Pearson, G., Milbrandt, J., Hansen, B., Platnick, S., Taylor, P., Gordon, M., Oakley, J. and Cober, S. (2009) The Fog Remote Sensing and Modeling field project. *Bulletin of the American Meteorological Society*, 90(3), 341–360.
- Philip, A., Bergot, T., Bouteloup, Y. and Bouysse, F. (2016) The impact of vertical resolution on fog forecasting in the kilometric-scale model AROME: A case study and statistics. *Weather and Forecasting*, 31(5), 1655–1671.
- Pilié, R., Mack, E., Rogers, C., Katz, U. and Kocmond, W. (1979) The formation of marine fog and the development of fog-stratus systems along the California coast. *Journal of Applied Meteorology and Climatology*, 18(10), 1275–1286.
- Pinty, J.-P. and Jabouille, P. (1998) A mixed-phase cloud parameterization for use in mesoscale non-hydrostatic model: Simulations of a squall line and of orographic precipitations, *Proceedings of the AMS conference on cloud physics*, Everett, WA (pp. 217–220). Boston, MA: American Meteorological Society.
- Price, J. (2011) Radiation fog. Part I: Observations of stability and drop size distributions. *Boundary-Layer Meteorology*, 139(2), 167–191.
- Price, J.D., Lane, S., Boutle, I.A., Smith, D.K.E., Bergot, T., Lac, C., Duconge, L., McGregor, J., Kerr-Munslow, A., Pickering, M. and Clark, R. (2018) LANFEX: A field and modeling study to improve our understanding and forecasting of radiation fog. *Bulletin of the American Meteorological Society*, 99(10), 2061–2077.
- Roquelaure, S., Tardif, R., Remy, S. and Bergot, T. (2009) Skill of a ceiling and visibility local ensemble prediction system (LEPS)

- according to fog-type prediction at Paris-Charles de Gaulle Airport. *Weather and Forecasting*, 24(6), 1511–1523.
- Savijärvi, H., Arola, A. and Räisänen, P. (1997) Short-wave optical properties of precipitating water clouds. *Quarterly Journal of the Royal Meteorological Society*, 123(540), 883–899.
- Seity, Y., Brousseau, P., Malardel, S., Hello, G., Bénard, P., Bouttier, F., Lac, C. and Masson, V. (2011) The AROME-France convective-scale operational model. *Monthly Weather Review*, 139(3), 976–991.
- Smith, D.K.E., Renfrew, I.A., Dorling, S.R., Price, J.D. and Boutle, I.A. (2021) Sub-km scale numerical weather prediction model simulations of radiation fog. *Quarterly Journal of the Royal Meteorological Society*, 147(735), 746–763.
- Steenefeld, G., Ronda, R. and Holtslag, A. (2015) The challenge of forecasting the onset and development of radiation fog using mesoscale atmospheric models. *Boundary-Layer Meteorology*, 154(2), 265–289.
- Tav, J., Masson, O., Burnet, F., Paulat, P., Bourriane, T., Conil, S. and Pourcelot, L. (2018) Determination of fog-droplet deposition velocity from a simple weighing method. *Aerosol and Air Quality Research*, 18(1), 103–113.
- Toledo, F., Haeffelin, M., Wærsted, E. and Dupont, J.-C. (2021) A new conceptual model for adiabatic fog. *Atmospheric Chemistry and Physics*, 21, 13099–13117.
- Vié, B., Ducongé, L., Lac, C., Bergot, T. and Price, J. (2022). Large-eddy simulation of LANFEX IOP1 radiative fog event: Prognostic vs. diagnostic supersaturation for CCN activation.
- Vié, B., Pinty, J., Berthet, S. and Leriche, M. (2016) LIMA (v1. 0): A quasi two-moment microphysical scheme driven by a multi-modal population of cloud condensation and ice freezing nuclei. *Geoscientific Model Development*, 9(2), 567–586.
- Vosper, S., Carter, E., Lean, H., Lock, A., Clark, P. and Webster, S. (2013) High resolution modelling of valley cold pools. *Atmospheric Science Letters*, 14(3), 193–199.
- Wagh, S., Krishnamurthy, R., Wainwright, C., Wang, S., Dorman, C.E., Fernando, H.J. and Gultepe, I. (2021) Study of stratus-lowering marine-fog events observed during C-FOG. *Boundary-Layer Meteorology*, 181(2), 317–344.
- Wilkinson, J.M., Porson, A.N., Bornemann, F.J., Weeks, M., Field, P.R. and Lock, A.P. (2013) Improved microphysical parametrization of drizzle and fog for operational forecasting using the Met Office unified model. *Quarterly Journal of the Royal Meteorological Society*, 139(671), 488–500.

**How to cite this article:** Fathalli, M., Lac, C., Burnet, F. & Vié, B. (2022) Formation of fog due to stratus lowering: An observational and modelling case study. *Quarterly Journal of the Royal Meteorological Society*, 148(746), 2299–2324. Available from: <https://doi.org/10.1002/qj.4304>

## APPENDIX A

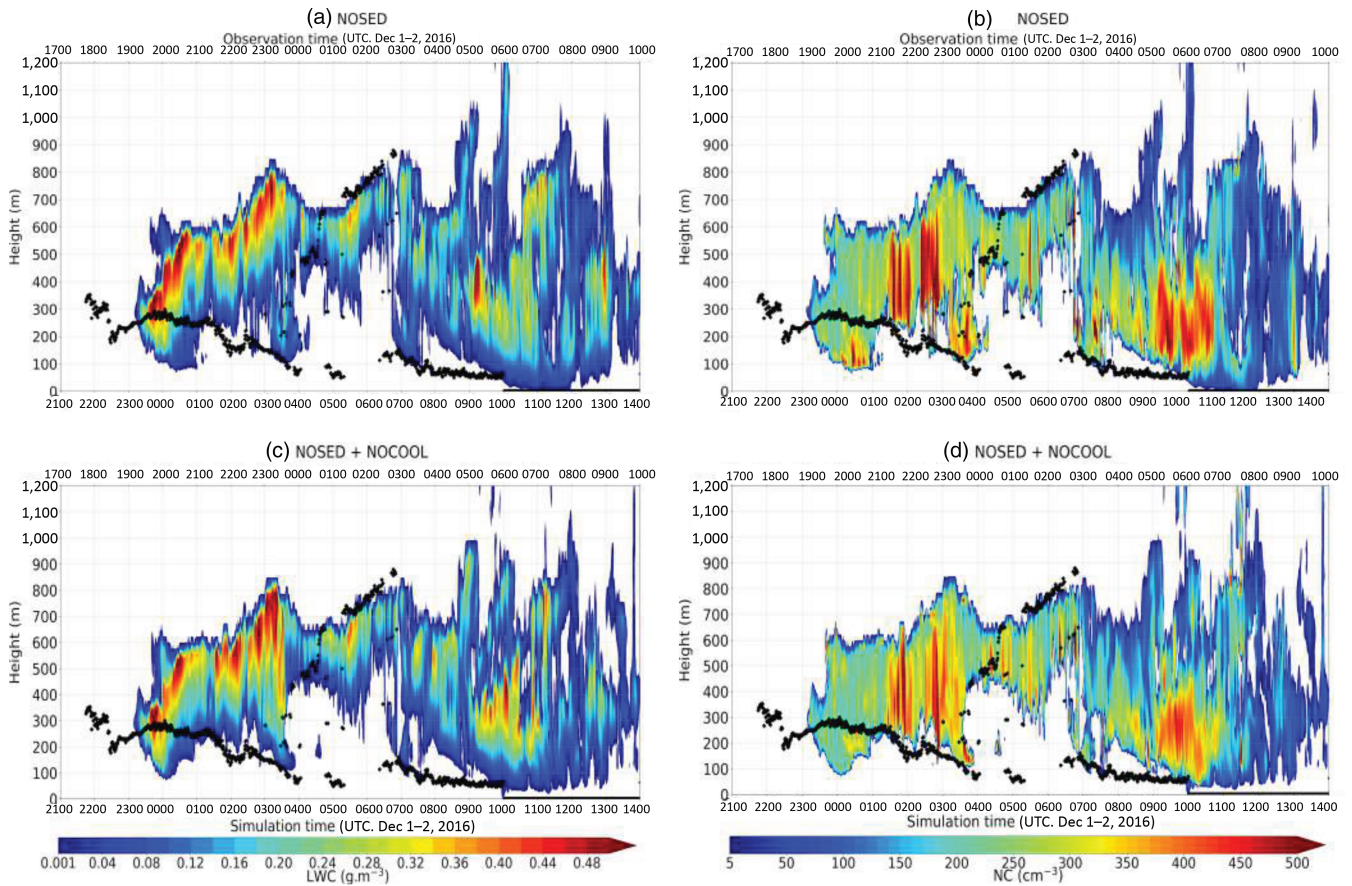


**FIGURE A1** Temporal evolution of vertical profiles at OPE of (a,c) liquid water content LWC ( $\text{g}\cdot\text{m}^{-3}$ ), (b,d) droplet number concentration NC ( $\text{cm}^{-3}$ ) for the NOSED and NOSED + NOCOOL simulations respectively. The real time axis of the measurements is at the top of the figures, and the time axis of the observations shifted by 4 hr corresponding to the time of the simulations at the bottom of the figures. Measurements of CBH are superimposed in black dots [Colour figure can be viewed at [wileyonlinelibrary.com](http://wileyonlinelibrary.com)]